NUMERICAL SIMULATION OF DROP BEHAVIOR USING PHASE-FIELD LATTICE BOLTZMANN METHOD

by

Zhe Chen

A thesis submitted in partial fulfillment of the requirements for the degree of

Master of Science

Department of Mechanical Engineering
University of Alberta

Abstract

In this study, we analysed numerically the behaviour of a liquid drop immersed into another immiscible liquid on a solid surface using a diffuse interface phase-field lattice Boltzmann method proposed by Mitchell et al. (Mitchell et al., 2018). The objective of the study is to assess the capabilities of the method when applied to several benchmarks. Special attention is given to the implementation of the wetting boundary condition, which poses a significant challenge in numerical modelling of a contact line motion.

For the first benchmark study, we placed a semi-circular droplet on a solid surface and let it equilibrate. The ability of the method to recover the static equilibrium contact angle achieved at different characteristics of the solid surface (from hydrophilic to hydrophobic) was assessed. The deviation between the numerical and analytical predictions in terms of the maximum height of the drop at the equilibrium state is within 3.3%.

Then, the simulations of a droplet sliding in a simple shear flow were performed to explore the capability of the method to capture the contact line motion. The numerical findings of the present work were compared to the reference data obtained by molecular dynamics simulation. The comparison showed a reasonable prediction for the receding angles, but not for the advancing angles. The possible reason and discussion are provided.

Acknowledgements

I would like to take this opportunity to express my gratitude to all the people who gave great help for my master studies in the Department of Mechanical Engineering at University of Alberta.

Firstly, I would like to give my most sincere gratitude and appreciation to my supervisor, **Dr. Alexandra Komrakova**, who gave me numerous kind and patient help not only on the academic and research areas, but also on my personal life and career development. She helped me pass through the tough transition when I first came here as an international student, and she always encouraged me to aim for the higher. I'm greatly impressed by her professionality as a scientific researcher, and greatly touched by her kindness personality. Without her continuous support and great guidance during the study and research period, I would not have the courage to conquer all the troubles I have met during the past two years and smoothly complete my master's degree.

Then, I would like to thank to my colleagues and friends, Wendy Zhang, Feiyu Jia, Yifei Bai, Cheng Zhong, and Kanishk Patel, for helping me through countless technical problems, for giving me wise suggestions for life and research, for treating me warmly like a family. I can't have such a meaningful and happy time in Edmonton without their encouragement and care.

Last but not least, I would like to express my deepest gratitude to my parents, Jiuwei Chen and Hongyu Li for their unconditional love and support over the years. They have always been my lighthouse and life model, which inspires me to go further and work harder. They respect all my decisions and listen to all my complaint without judgment, they made who I am today.

Table of Contents

List of Tables

List of Figures

List of Symbols

A	surface area
A_0	initial mass per unit density of the drop
a	the parameter related to contact angle
c	ratio of lattice time and length scale
c_s	speed of sound
e_α^g	lattice structure velocity sets for D3Q27 model
e_α^f	lattice structure velocity sets for D3Q15 model
f_1, f_2	fraction of different surfaces
f_α, g_α	particle distribution functions after collision
$f_\alpha^\star, g_\alpha^\star$	particle distribution functions
${f_\alpha}^{eq}, {g_\alpha}^{eq}$	equilibrium particle distribution functions
$\bar{f}_\alpha^{eq}, \bar{g}_\alpha^{eq}$	modified equilibrium particle distribution functions
$\mathbf{F}$	volumetric force
$\mathbf{F}_s$	surface tension force
$\mathbf{F}_b$	body force
$\mathbf{F}_p$	pressure force
$\mathbf{F}_\mu$	viscosity force
$\mathbf{F}_{LG}$	interface tension force of liquid-gas phase
$\mathbf{F}_{SL}$	interface tension force of solid-liquid phase
$\mathbf{F}_{SG}$	interface tension force of solid-gas phase
F_α	hydrodynamics forcing for f_α
${F_\alpha}^\phi$	hydrodynamics forcing for g_α
$\mathbf{g}$	gravitational acceleration
G	shearing rate
h	half of the distance of lattice nodes
k_{end}, k_{sta}	location of parallelized sub-domain
l	frame length in surface tension measurement experiment

M	mobility
n	number of molecules
nx	simulation domain length in x-direction
ny	simulation domain length in y-direction
nz	simulation domain length in z-direction
$\hat{\mathbf{n}}$	normal vector
$\hat{\mathbf{n}}_w$	normal vector at the wall
p	pressure
p^*	normalised pressure
S_1, S_2	different chemical type of the surfaces
$\hat{S}$	diagonal relaxation matrix
R	droplet radius
R_0	initial droplet radius
T	temperature
U	macroscopic drop velocity
$\mathbf{u}$	lattice units drop velocity
v	velocity of the moving walls
V	volume
W	the needed energy for surface tension measurement experiment
x	x direction
y	y direction
z	z direction

Greek letters

β	coefficient related to surface tension and interface thickness
δx	lattice units length scale
δt	lattice units time scale
$\lambda(x)$	solution variable for finite volume method
$\bar{\lambda}_i$	approximate average solution value for finite volume method

∇	gradient
∇^2	Laplcian
θ	contact angle
θ_1	intersection angle
θ_r	receding angle
θ_a	advancing angle
Θ	parameter related to contact angle
κ	coefficient related to surface tension and interface thickness
κ_{CL}	capillary length
μ	dynamic viscosity
μ_ϕ	chemical potential
μ_H	viscosity for the heave fluid
μ_L	viscosity for the light fluid
ν	kinetic viscosity
ξ	interface thickness
Ω_α	collision operator
ω_α^f	lattice weights for D3Q27 model
ω_α^g	lattice weights for D3Q15 model
ρ	density
σ	surface tension
τ	relaxation time for weighed Multiple-relaxation-time operator
τ_ϕ	relaxation time for Bhatnagar-Gross-Krook operator
τ_H	relaxation time for the heavy fluid
τ_L	relaxation time for the light fluid
ϕ	order parameter
ϕ_H	order parameter for the heavy fluid
ϕ_L	order parameter for the light fluid
ϕ_0	order parameter for the interface

$\phi_i{}^{(1)}$	order parameter at the nearest point
$\phi_i{}^{(2)}$	order parameter at the second-nearest point
$\phi_i{}^{(3)}$	order parameter at the third-nearest point

Subscripts

α, β	lattice population direction
H, L	heavy fluid and light fluid
i, j, k	x, y, z coordinates
LS	liquid-solid phase
LG	liquid-gas phase
SG	solid-gas phase

Dimensionless numbers

Ca	capillary number
Re	Reynolds numberd
R_0/h	dimensionless of distance

Abbreviations

BC	boundary condition
BGK	Bhatnagar-Gross-Krook
FD	finite difference
FDM	finite difference method
FEM	finite element method
FVM	finite volume method
LBE	lattice Boltzmann equation
LBM	lattice Boltzmann method
lu	lattice unit
MAC	marker-and-cell
MD	molecular dynamics

MPI	message-passing interface
LBM	lattice Boltzmann method
PDE	partial difference equation
VOF	volume-of-fluid
WMRT	weighed multiple-relaxation-time

Chapter 1

Introduction

1.1 Motivation

Numerous chemical, biological, food, and pharmaceutical engineering processes involve emulsion flow. An emulsion is a mixture of two or more liquids that are typically immiscible. In emulsion, one liquid (the dispersed phase) is dispersed into the other (the continuous phase). Consider water flooding as an enhanced oil recovery method as an example: water is injected into the rock formulations containing oil, and inclusion will be washed away as water enters into the oil mixture and forms an emulsion system (Sheng, 2014). Predicting the success of oil recovery process is difficult because of the complexity of the rock structure, the continuous interaction between the pore walls and the fluid, and the interfacial effects between the water and the oil phase (Desmond et al., 2017). Therefore, evaluating the performance of such system requires a thorough understanding of the multiphase system and drop-wall interaction. Other engineering applications for emulsion flow include high-performance heat exchangers (Faghri and Zhang, 2006), polymer processing (Han, 2012) and microfluidics (Günther and Jensen, 2006). It is of great industrial importance to understand the physics behind such system and obtain a method allowing to perform a quantitative analysis of it.

Multiphase flow, which is distinguished from a single-phase flow by the presence of one or more interfaces separating the phases, can be considered as a field that is divided into single-phase regions by the interfaces or moving boundaries between phases (Faghri and Zhang, 2006). The interfaces can be created by the existence of a physical state (gas, liquid, solid) or two immiscible fluids. The focus of the present work is consideration of the system of two immiscible liquids and its interaction with the solid surface. For instance, emulsion dispersion pipe flow that occurs during co-

current flow of two immiscible liquids such as oil and water (Arirachakaran et al., 1989). Along with the complexity of the multiphase flow on its own, we want to understand what happens with this flow as it approaches the wall. Therefore, we are interested in behaviour of drops dispersed in another immiscible liquid when they approach and make contact with the wall.

The ability of the liquid drop to maintain the contact with the solid surface is called surface wetting. Surface wetting phenomenon is widely encountered and is of great significances in numerous industrial applications. This includes full wetting and adhesion (Good, 1992), partial wetting and printing plates (Brochard-Wyart and De Gennes, 1992), and non-wetting and water-proofing (Ma and Hill, 2006).

The exploration of surface wetting was initialized by Thomas Young at the 18^{th} century and has been under constant development since then. Early researchers tried to understand the surface wetting and contact line motion using experiments. For example, they studied the wetting on polymer surfaces (Geoghegan and Krausch, 2003), wetting on textured surfaces (Geoghegan and Krausch, 2003), and wetting on surfaces with different roughness (Zhou and De Hosson, 1995). They generally gave their attention to macroscopic scale change of the liquid behavior when it contacts with different solid surfaces, and failed in capturing the actual physical process of drop-wall interaction. One of the possible reasons might be that liquid-liquid-solid interaction (in this thesis, the liquid-liquid-solid system refers to two immiscible fluid that contacts with a solid surface) is a complex process that occurs on multiple length and time scales. Take turbulent emulsion flow in a static mixer as an example. During this process, emulsion flow is formed and liquid-solid interaction also continuously happens. In the system, the thickness of interface between the phases is approximately *Å*ngstrom, drop diameter is around 0.1 to 500 μm, while the macro length scale of the mixer can be several inches. The drops frequently collide with the surface and break within milliseconds, while it takes hours for the system to reach the equilibrium state. Capturing the process over entire range of scales is challenging.

An alternative approach to study multiphase systems is to perform numerical simulations. Numerical simulation has certain advantages over experiments in the following aspects: highly resolved simulations can capture the microscopic process on a scale of a single-drop up to the macroscopic processes of dispersed and continuous phases evolution; simulations can change the flow domain without the cost of redesigning the entire equipment as experiments do; simulation allow us to visualize systems in much greater detail than experiments, and the simulation length scale can normally go beyond the existing experimental capabilities.

The main goal of the present research is to develop a numerical method to study the surface wetting phenomena and contact line motion for a liquid-liquid-solid system. The choice of the method is important and will be discussed and justified later. For the following chapters, we briefly go through some existing methods and current challenges, then present our choice of the numerical method with reasoning behind.

1.2 Numerical Challenges for Interface Modelling

There are two main categories of the approaches to simulate multiphase flows, which are interface tracking and interface capturing approaches. Interface tracking requires Lagrangian marker points to explicitly track the interface. For such methods, including marker-and-cell (MAC) (McKee et al., 2008) and front-tracking methods (Tryggvason et al., 2011), the computational mesh elements lay in part or fully on the fluid-fluid interfaces (Mirjalili et al., 2017). This gives the interface tracking method a great accuracy because the equations and interface boundary conditions are applied exactly without any simplification. In interface capturing methods, on the other hand, the mesh elements do not lay on the interface, but rather the interface evolves through the mesh. The common interface capturing methods include volume-of-fluid (VOF) (Sussman and Puckett, 2000), level-set (Osher and Fedkiw, 2001), and phase-field methods (Yabe et al., 2001).

Sharp interface method and diffuse interface method are two common methods to describe the interface. Sharp interface method considers the interface between two immiscible fluids to have a zero thickness. Diffuse interface method presumes that the interface between the phases is not sharp, but has a finite thickness and is characterized by rapid but smooth transitions in density ρ, viscosity μ and other physical parameters (Sun and Beckermann, 2007). The fluid properties profile for the sharp interface and diffuse interface method is shown in Fig.1.1.

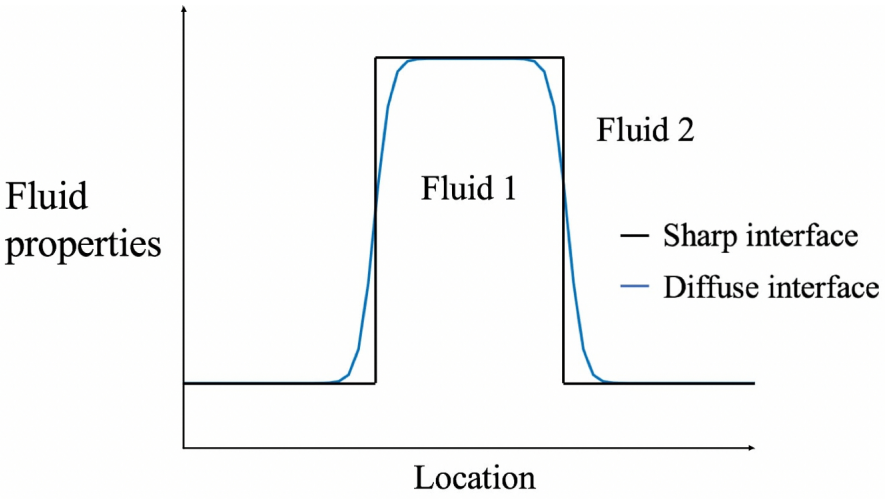

Figure 1.1: Fluid properties profile for the sharp interface and diffuse interface methods

Due to the intrinsic characteristic of the interface tracking approaches, these methods belong to the sharp interface methods. A part of the interface capturing methods also belongs to the sharp interface methods, including the aforementioned VOF (Sussman and Puckett, 2000) and level-set methods (Osher and Fedkiw, 2001). Various publications have described in detail how a sharp interface model can be efficiently implemented, which include the one on volume-of-fluid (Wang et al., 2009), on front-tracking (Tryggvason et al., 2001), and on the immersed boundary (Peskin, 2002) methods. For sharp interface method, the interface is a two-dimensional boundary and is usually represented by a distinct computational mesh, so the motion of this interface needs to be explicitly tracked, and a Navier-Stokes solver is required on either side of the interface. This leads to a high cost in terms of computational efficiency because that means tracking the interface needs a mathematical reconstruction for every time step.

Another challenge posed by the sharp interface method is the existence of singularity in the flow variables when the interface interacts with a solid phase. Take velocity singularity as an example (Yue and Feng, 2011). Consider the red circle point shown in Fig.1.2. This point is located at the interface. If the drop has a velocity U, this circled point should move along with the drop and also have a velocity term U. On the other hand, this point is adjacent to the static solid wall and, therefore, has to satisfy the no-slip boundary condition. This leads to a singularity point, as one point cannot have two velocities.

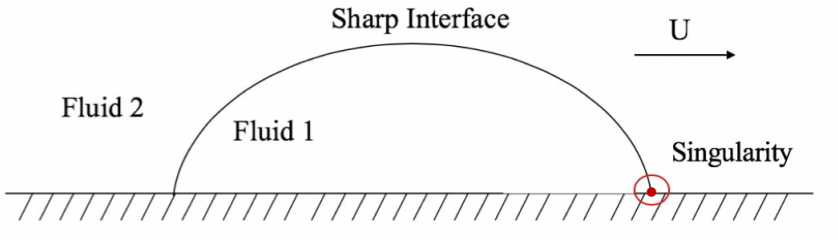

Figure 1.2: Sharp interface model. Red circle presents the velocity singularity at the interface

To overcome the singularity problem, one common approach is to insert a slip velocity boundary to an adjacent region of the contact line (Kusumaatmaja et al., 2016). Spelt et. al (Spelt, 2005) used a level-set method to simulate the moving contact lines of binary fluid system with equal densities. They successfully avoided the singularity by replacing the no-slip condition with a velocity component defined by the moving wall velocity. Other possible approach is to place a precursor thin film ahead of the contact line (Pismen and Pomeau, 2000) (Eggers, 2005).

The diffuse interface method has the intrinsic capacity to avoid the singularity problem, because the fluid discontinuities are smoothed via interface thickness and the surface tension force is diffused over a thin layer near the interface to become a volume force. Surface tension force is the incentive of singularity formulation for the sharp interface method. Another important advantage of the diffuse interface methods is that they do not require mesh 'ad hoc' cut-and-connect operations since the interface is not represented by computational mesh. Instead it evolves through the mesh, as shown in Fig.1.3.

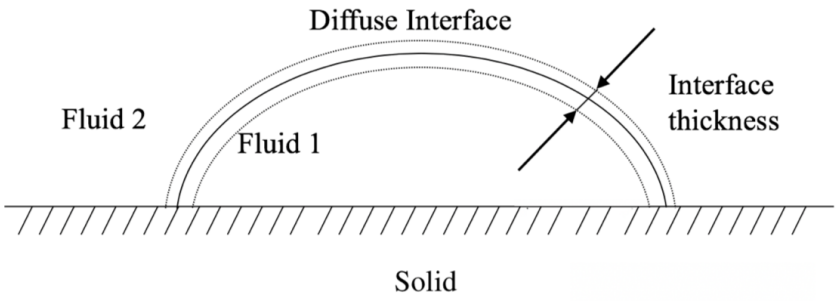

Figure 1.3: Diffuse interface model

However, the selection of the interface thickness is not trivial since the diffuse interface thickness cannot be chosen as small as in reality due to the computational restrictions (Khatavkar et al., 2006), while larger interface thickness might lead to inconsistency between the numerical and experimental results. Therefore, only when the interface thickness approaches a specific length scale, so-called sharp interface limit, it can represent the reality (Xu et al., 2018).

We can see that sharp interface method is a powerful method but have difficulty simulating through and past the transitions brought by the interfaces and solid wall. This makes it challenging to simulate the multiphase systems, especially the ones with drop-wall interaction as the aforementioned liquid-liquid-solid system. The diffuse interface methods also have numerical challenges, such as the interface thickness, but for this study, we chose to use the diffuse interface method in terms of computational efficiency, stability, and accuracy.

Several diffuse interface models have been studied to handle the three-phase moving contact line dynamics (Rowlinson and Widom, 2013) (Jacqmin, 2000) (Jamet et al., 2001). Among all the possible choices, phase-field method is widely used (Sun and Beckermann, 2007) because it has several important advantages over other methods. Phase-field method uses an order parameter ϕ to represent the different phases in the system. The transport equation governing the order parameter is modified by incorporating physical effects that govern thin interfaces (Mirjalili et al., 2017). Except for its ability to implicitly track the interface, it is also an Eulerian variable defined in the flow domain, which allows phase-field method to easily adapt efficient solvers and be parallelized. Unlike interface-tracking methods, phase-field model is an interface-capturing method and, thus, benefits from a reduced computational cost because there is no need to track the interface deformation and extension.

Traditionally, the phase-field methods are either based on the Cahn-Hilliard or the Allen-Cahn equations to describe the time or space evolution of the phase field parameter ϕ. These are two important gradient flows of the Ginzburg-Landau-Wilson free energy functional (Mirjalili et al., 2017). In these two equations, the Cahn-Hilliard equation can provide the mass conservation, but a fourth-order derivative that rises in taking the Laplacian of the chemical potential might lead to instability and reduce the accuracy of numerical approximations (Fakhari and Bolster, 2017). The Allen-Cahn equation, on the other hand, only handles the term with the second-order derivation, but the total mass cannot be conserved (Mirjalili et al., 2017). This has motived researchers to look for an equation that can combine the advantages of both equations.

In our research, we use a conservative phase-field method introduced by (Mitchell et al., 2018). Motivated by the Allen–Cahn equation, Sun and Beckermann (Sun and Beckermann, 2007) proposed a second-order PDE suitable for the two-phase simulations for curvature-driven flow. Chiu and Lin (Chiu and Lin, 2011) was later on inspired by conservative-level-set method and reformulated the phase field method proposed by Sun and Beckermann to a conservative form. The description of the conservative phase-field equation used here will be given in Chapter 2.

1.3 Numerical Methods to Solve Governing Equations

After outlining the approach to solve the problem, the next step is to find a powerful numerical method to solve the governing equations. There are many numerical methods that can be used to solve the governing equations for the multiphase system. Generally, these methods can be classified into two categories. The first category is the conventional numerical methods that are based on discretising the equations of fluid mechanics, such as finite difference, finite volume, and finite element methods. The second category is the methods that are based on microscopic, mesoscopic, or macroscopic particles, such as molecular dynamics, lattice gas models, and multi-particle collision dynamics (Krüger et al., 2017).

Conventional methods work on directly solving the governing equations and coming up with a solution consisted of approximation term. The set of governing equations normally includes continuity equation, Navier-Stokes equations and any other additional equation (phase-field equation, in our case).

In the finite difference method (FDM), physical space is divided into a regular grid of nodes. The principle of this method is to replace all the derivatives in the equations by a finite difference approximation (Krüger et al., 2017). Although the logic is simple, these are certain weakness inherent to this method: normally there are several coupled unknowns in the set of governing equations, which makes the implementation of FDM more complex; due to the existence of numerical errors, the conservation of mass, momentum and energy cannot be guaranteed; and since finite difference method is normally based on a regular grid, and therefore it is not suitable to solve flow fluid with complex geometries (Ferziger and Peric, 2012).

In the finite volume method (FVM), space does not need to be divided into a regular grid. Instead, we subdivide the simulated volume V into many smaller control volumes V_i, which may have different sizes and shapes to each other (Ferziger and Peric, 2012). This gives it the flexibility of dealing with complex geometry. In the middle of each finite volume V_i, there is a node where each solution variable $\lambda(x)$

is represented by its approximate average value $\bar{\lambda_i}$ within that volume. The finite volume method is designed to solve conservation equations, and this gives FVM the instincts of being conservative (Krüger et al., 2017). Researches aiming at improve the accuracy of FVM can be found in (Moukalled et al., 2016).

In finite element methods (FEM), partial differential equations (PDE) are solved using an integral form equation, where the PDE itself is multiplied with a weight function $\omega(x)$ and integrated over the domain of interest. Each grid for FEM has a discretised solution variable and the variable can be interpolated through given conditions. The advantages for FEM include that it can be easy to achieve high order accuracy and it is well equipped for unstructured grid. But just as FDM, it is not conservative and it is way more complex than FDM and FVM. The 'checkerboard instabilities' might also show up for FEM if not deliberately designed to avoid (Krüger et al., 2017).

Particle-based methods are not based on directly discretising the equations of fluid mechanics, but they represent the fluid using particles. Depending on the specific method, a particle may represent an atom, a molecule, a collection of molecules, or a portion of the macroscopic fluid. Thus, while conventional Navier-Stokes solvers take an entirely macroscopic view of a fluid, particle-based methods usually take a microscopic or mesoscopic view.

Molecular dynamics (MD) (Frenkel and Smit, 2002) is probably one of the most commonly used particle-based methods. It tracks the position of atoms or particles and use accumulation behavior to reflect the flow field. Coninck et. al (De Coninck and Blake, 2008) did a concise research on the molecular dynamics simulations of liquid drop wetting. They studied the droplet wetting ability for a liquid-liquid-solid system, together with drop spreading on a flat surface and fibers surface. The dynamic contact angle was also given a special attention.

Besides molecular dynamics, lattice gas models (Rivet and Boon, 2005), dissipative particle dynamics (Hoogerbrugge and Koelman, 1992), multi-particle collision dynamics (Malevanets and Kapral, 1999) (Malevanets and Kapral, 2000) and smoothed-particle hydrodynamics (Gui-rong, 2003) are all nowadays prevailing particle-based methods. These methods vary in methodology and interface-describing strategies, and are often tailored to some kind of particular problems. It is, therefore, difficult to give a general summary of these methods as a whole. However, some particle-based methods have difficulty in making connection with the macroscopic description of a fluid (Krüger et al., 2017). Thus makes it even more difficult to be evaluated through experiments or other numerical simulations.

Lattice Boltzmann method (LBM) (Ladd, 1994) is a mesoscopic method. Instead of directly tracking the atoms, particles, small fluid volume (microscopic methods) or directly solving general governing equations (macroscopic methods), it tracks the particle distribution function and uses the collective behavior of particles to represent the entire fluid. In LBM, fluid volume is discretized in physical and velocity spaces. Fictious particles are allowed to move through collision and streaming process in certain directions so as to update the particle distribution function after each time step. In LBM scheme, particles have certain distribution and movement pattern, the commonly used are D2Q9, D3Q15, D3Q19, and D3Q27 model, where D stands for dimension and Q provides a number of velocity direction.

Lattice Boltzmann methods have been successfully used in resolving the diffuse interface method and modelling multiphase system regarding contact line motion problems in recent years. Examples include the studies of droplet formation in T-shape channel (Van der Graaf et al., 2006), droplet impacting (Ma et al., 2018), droplet spreading and sliding (Derksen and Komrakova, 2019).

LBM is a powerful and efficient method for multiphase flow simulation. For solving the incompressible Navier-Stokes equation, the LBM takes the advantage of simplicity and scalability (Nourgaliev et al., 2003). It is conservative and suitable for complex geometry simulation, it is grid-based so it can be easily parallelized. At the same time, LBM is memory-intensive as the populations for each point of the domain need to be stored and updated separately.

In conclusion, different solvers have different advantages and disadvantages, certain problems might need a specific method in order to accomplish an efficient simulation. It is agreed by researchers that there is no one method which is superior to all others. In our research, we chose to use LBM because of its suitability for the multiphase flow simulation.

1.4 Literature Review on Relevant LBM Simulations

Historically, there are four major classes of lattice Boltzmann models for multiphase flows interacting with a solid phase. They are the color gradient model (Gunstensen et al., 1991), the pseudopotential model (Shan and Chen, 1993) (Shan and Doolen, 1995), the free-energy model (Swift et al., 1995) and the mean-field model (He et al., 1999). For most of the applications, these previous models suffered from the numerically unphysical problem or a lack of Galilean invariance, and large spurious velocities (Fakhari et al., 2017b). During the past decades, these models have been under constant improvements and new LB models have also been proposed to deal with the listed deficiencies.

In this section, we briefly go through some recent publications that report the results of studies of the surface wetting phenomenon or contact line motion. In particular, we focus on implementation of liquid-liquid-solid system and the way the wetting boundary condition are applied.

Leclaire. et al (Leclaire et al., 2016) used a color gradient model to preform a two-dimensional multiphase flow simulation, in order to test its ability to capture the equilibrium static contact angle. A wetting boundary condition is proposed and consisted of directly imposing the contact angle at the boundaries in much the same way as the Dirichlet boundary conditions do. To achieve that, color gradient and density gradient at the location near the solid lattices need to be calculated. Although the proposed wetting boundary condition and coupled LBM produced good agreement with the simulated contact angle and Young's equation, the scheme has difficulty in expanding to three-dimensional simulation in terms of computational cost.

In order to deal with the large spurious currents at the fluid-solid surface, Leclaire. et al (Leclaire et al., 2015) published another work on scaling the interfacial thickness with the grid resolution. Other researchers also worked on improving the stability of the color gradient model application in this area (Liu et al., 2012) (Ba et al., 2016).

Briant et. al (Briant and Yeomans, 2004) studied the contact line motion in binary fluids with a free-energy LBM. They focused on how the contact line singularity can be overcome by diffusion over a length scale at the contact line. They also derived a scaling form for the dependence of the length scale on system parameters. In order to implement the wetting boundary condition, they added a surface term to the free energy and then by minimizing the free energy, an equilibrium boundary condition which directly related to the wetting contact angle was given.

Pooley. et al (Pooley et al., 2008) considered the contact line dynamics in binary fluids with a viscosity ratio of 12.5 using the free-energy LBM. The wetting boundary condition was applied by altering the gradient of order parameter ϕ at the solid wall, which is an exact result obtained through minimizing a free-energy expression. They proved that using free-energy LBM, coupled with a single-relaxation-time collision operator, will cause spurious currents arise in the system and make the contact line dynamics hard to capture. They proposed a revised lattice Boltzmann method, based on a multiple-relaxation-time algorithm, and showed that the method has superiority over numerical accuracy with theory, both for the capture of equilibrium contact angle, and for the advancing contact angle, measured in capillary filling simulations.

Researches have also given their focuses to the wetting boundary condition implementation coupled with a phase-field LBM.

Lee et. al (Lee and Liu, 2010) proposed a phase-field lattice Boltzmann method for incompressible binary fluids to model the contact line dynamics on partially wetting surfaces. The wall boundary conditions for both the particle distribution functions and the intermolecular forcing terms were proposed and they were derived based on the minimization of the free energy. They proved that the presented LBM was capable of eliminating the parasitic currents to machine accuracy in the presence of a wall boundary. The proposed boundary conditions were also capable of reproducing the theoretical values of the contact angles for moderate equilibrium contact angles, although become less accurate for very high contact angles.

Liu et. al (Liu et al., 2014) developed a phase-field lattice Boltzmann model to simulate thermocapillary flows in a confined microfluidic geometry. An interfacial force of potential form was proposed to model the interfacial tension forces and because only the first-order derivatives are involved in the scheme, the interfacial force of potential form can be easily combined with a cubic wetting boundary condition to account for the fluid–surface interactions. The cubic wetting boundary condition was also an approximation energy minimization from, which neglected some higher-order terms in the free-energy function (Lee and Liu, 2010). In their research, the hydrodynamic equations are solved with a multiple-relaxation-time collision operator, which enhanced the numerical stability for solving a binary fluid with large viscosity difference and produce correct equilibrium contact angles.

A study by Huang et. al (Huang et al., 2015) compared five different wetting boundary conditions for the phase-field lattice Boltzmann method. Among the five wetting boundary conditions, three used the linear, cubic, and sine form surface energy, while the other two used the geometric formulation and the characteristic

interpolation. It was found that although all wetting boundary conditions can predict the static contact angle accurately, the performances on the capture of contact line motion varied with the setting of initial contact angle. Besides, a new implementation that may be used for all wetting boundary conditions was proposed to mimic the wall energy relaxation and control the degree of slip, which helped the model to match experimental measurements better.

Some other boundary conditon implementations can also been found at a work published by Jahanshaloo (Jahanshaloo et al., 2016).

Fakhari et al (Fakhari and Bolster, 2017) presented a three-phase contact line dynamics work using a conservative phase-field LBM. They introduced a simple and efficient lattice Boltzmann scheme for immiscible multiphase flows, and proposed a new algorithm for specifying the three-phase contact angle on solid boundaries within the framework of structured Cartesian grids. The proposed method has superior computational accuracy and efficiency compared to the common approaches which neither require an approximation from the free-energy expression nor a geometric formula. The validation cases were achieved through simulations on wetting and dewetting on a flat surface, on a cylindrical surface, and a droplet falling on hydrophilic and superhydrophobic circular cylinders. The method was proved to be powerful and promising. However, only two-dimensional situations were considered and there were no cases accomplished on the capture of the contact line motion. Both these issues presented important further research values.

From the literature review, we can see that at the moment, few researches looked into the wetting boundary condition implementation for a phase-field LBM without considering the minimization of free-energy expression nor a geometic formula. If any, they hardly focused on three-dimensional cases nor contact line motion capturing. Therefore, it is important to expand the wetting boundary condition introduced by (Fakhari and Bolster, 2017) to the three-dimensional cases and study its ability to capture the equilibrium state contact angle, as well as contact line motion.

1.5 Objective

The main goal of the present research is to develop a numerical framework that can be used to study a drop behavior on a surface for a liquid-liquid-solid system. We use a conservative phase-field lattice Boltzmann approach proposed by (Mitchell et al., 2018) to investigate surface phenomena and contact line motion. Two studies are performed and discussed in Chapter 3 and Chapter 4 of the thesis. All codes were written in Fortran and were developed from scratch. The relative parallelization work was also accomplished.

In Chapter 2, we give a detailed description of the numerical method we used. Macroscopic governing equations are introduced and the lattice Boltzmann formulation to solve these equations is provided. In particular, we focus on the implementation of wetting boundary conditions in Chapter 2.3 and provide a code workflow.

In Chapter 3, we applied the lattice Boltzmann method to study the surface wetting phenomena. A semi-circular liquid drop is placed on a solid surface and waited to reach its equilibrium state, then the contact angle and the maximum height of the drop is measured and compared with the theoretical solutions. By achieving such simulations, we are able to validate the current method to capture the static contact angle.

In Chapter 4, we validate the model's ability to capture the contact line motion. Three cases were completed by applying numerical studies of drop sliding cases between two parallel solid plates. We first placed a semi-circular liquid drop to the surface and waited it to reach the equilibrium state, then started to shear the walls. During the process, we observed the deformation and measured the receding and advancing angle, the simulated results were compared to a reference data achieved by molecular dynamics simulation.

Chapter 5 contains conclusions and outlook for the future work. There are also four appendices, including the two-dimensional case we studied as a starting point.

Chapter 2

Numerical Method

In this chapter, a detailed description of the numerical method used in the present study is presented. The governing equations of the incompressible, multiphase flow are introduced followed by a lattice Boltzmann framework proposed by (Mitchell et al., 2018) to solve these equations. This approach is built on the improvement of Zu and He's method (Zu and He, 2013) to improve efficiency and numerical stability. An interface-capturing equation based on the conservative phase-field model is employed to capture the interface. A velocity-based lattice Boltzmann equation (LBE) is used to capture hydrodynamics. The method has many advantages over efficiency, accuracy and stability: only one non-local variable is introduced in the applied model (order paramter ϕ), for which finite-difference (FD) scheme is needed to calculate its derivatives. Reducing the non-locality in the system greatly improves its parallelization ability. For the FD scheme, instead of using biased or mixed (centered and biased) difference FD schemes as many free-energy models do (Lee and Liu, 2010), we use a second-order, isotropic centered differences introduced by (Kumar, 2004) (Ramadugu et al., 2013) (Thampi et al., 2013) to increase the model stability, as mixed difference FD might affect mass and momentum conservation (Guo et al., 2011). A simplified equilibrium distribution is used in order to decouple pressure and velocity calculations. For the previous study (Zu and He, 2013), the velocity and pressure are coupled, which requires a complex predictor-corrector scheme. The superiority of the applied method will be discussed in detail in the following sections.

2.1 Macroscopic Equations

2.1.1 Governing Equations

The governing equations for the incompressible multiphase system are defined as

$$\nabla \cdot \mathbf{u} = 0 \tag{2.1a}$$

$$\rho\left(\frac{\partial \mathbf{u}}{\partial t} + \mathbf{u}\cdot\nabla\mathbf{u}\right) = -\nabla p + \nabla\cdot(\mu[\nabla\mathbf{u} + (\nabla\mathbf{u})^{\mathrm{T}}]) + \mathbf{F} \tag{2.1b}$$

$$\frac{\partial \phi}{\partial t} + \nabla\cdot(\phi\mathbf{u}) = \nabla\cdot M\left(\nabla\phi - \frac{1-4(\phi-\phi_0)^2}{\xi}\hat{\mathbf{n}}\right) \tag{2.1c}$$

Eq.(2.1a) and eq.(2.1b) are the continuity and momentum equations, respectively (Badalassi et al., 2003) (Ding et al., 2007) (Li et al., 2012) (Kendon et al., 2001).

Here ρ and μ are the fluid density and viscosity respectively; p is the pressure, $\mathbf{u}$ is the macroscopic velocity vector, t is the time, term $\mu[\nabla\mathbf{u} + (\nabla\mathbf{u})^{\mathrm{T}}]$ is the viscous stress tensor, and $\mathbf{F} = \mathbf{F}_s + \mathbf{F}_b$ is the volumetric force. The terms $\mathbf{F}_s$ and $\mathbf{F}_b$ represent the forces associated with the surface tension and the body forces in the system, respectively. In this work, surface tension force $\mathbf{F}_s$ is calculated as (Jacqmin, 1999)

$$\mathbf{F}_s = \mu_\phi \nabla\phi \tag{2.2}$$

with the chemical potential μ_ϕ for the binary fluids being defined as (Mitchell et al., 2018)

$$\mu_\phi = 1.5\sigma\left[32\phi(\phi-1)(\phi-0.5)/\xi - \xi\nabla^2\phi\right] \tag{2.3}$$

where σ is the surface tension, ξ is the interface thickness.

The body force $\mathbf{F}_b$ is calculated as

$$\mathbf{F}_b = \rho\mathbf{g} \tag{2.4}$$

where $\mathbf{g}$ is the gravitational acceleration.

Eq. (2.1c) is used to capture the interface between the phases. As introduced before, previous phase-field methods are either based on the Cahn-Hilliard or the Allen-Cahn equations. For our model, we adapt a conservative phase-field method introduced by (Chiu and Lin, 2011). The method came from the development of Sun and Beckermann's method (Sun and Beckermann, 2007). Chiu and Lin (Chiu and Lin, 2011) further improved the method and reformulated Sun and Beckermann's method to a conservative form. In this method, the phase field ϕ takes two extreme values, ϕ_H and ϕ_L, standing for the heavy and light fluid; $\phi_0 = (\phi_H + \phi_L)/2$ stands

for the interface. In eq.(2.1c), M is the mobility, and $\hat{\mathbf{n}}$ is the unit vector normal to the surface, pointing out of the heavy fluid:

$$\hat{\mathbf{n}} = \frac{\nabla\phi}{|\nabla\phi|} \tag{2.5}$$

The equilibruim profile of the phase field for an interface at location $\mathbf{x}_0$ is written as (Mitchell et al., 2018)

$$\phi(x) = \phi_o \pm \frac{\phi_H - \phi_L}{2}\tanh\left(\frac{\mathbf{x} - \mathbf{x}_0}{\xi/2}\right) \tag{2.6}$$

This equation is normally used to set the initial condition for the phase field. The $\pm$ sign is chosen such that the minimum value of the phase field is assigned to the light fluid. In our case, we assigned $\phi = 0$ to the light fluid and $\phi = 1$ to the heavy fluid, and $\phi = 0.5$ indicates the interface between phases, as shown in Fig 2.1. After rearranging eq. (2.6), we have

$$\phi(x) = \frac{1}{2}\left[1 - \tanh\left(\frac{|\mathbf{x} - \mathbf{x}_0|}{\xi/2}\right)\right] \tag{2.7}$$

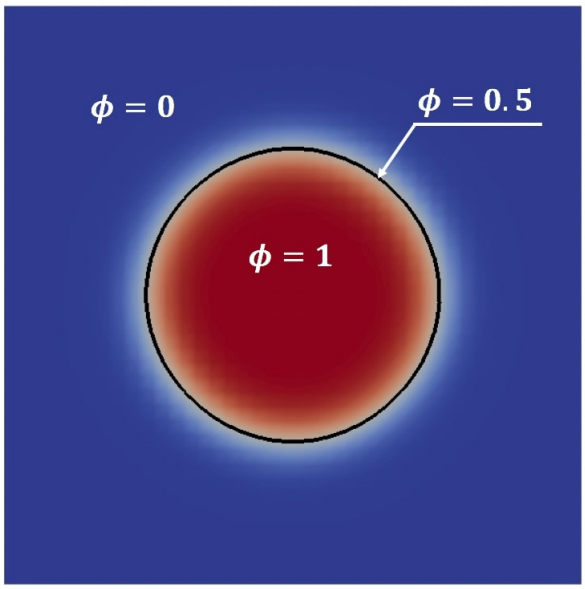

Figure 2.1: The distribution of the order parameter ϕ for a phase field method

2.1.2 Wetting Boundary Condition

When the fluid interacts with a solid surface and imposes a non-neutral contact angle at the solid boundary, we have the following boundary condition (Jacqmin, 2000)

$$\hat{\mathbf{n}}_W \cdot \nabla\phi|_{x_W} = \Theta\phi_W(1-\phi_W) \tag{2.8}$$

where $\hat{\mathbf{n}}_W$ is the unit factor normal to the solid wall, pointing away from the heavy fluid. ϕ_W is the phase-field at the solid wall, and Θ is a parameter that related to the contact angle by

$$\Theta = -\sqrt{\frac{2\beta}{\kappa}}\cos\theta \tag{2.9}$$

Coefficients β and κ can be calculated from the surface tension σ and the interface thickness ξ as

$$\beta = 12\sigma/\xi \tag{2.10a}$$

$$\kappa = 3\sigma\xi/2 \tag{2.10b}$$

For fluids with neutral wetting conditions (90°) or no interaction with solid walls, the wetting condition can be simplified as

$$\hat{\mathbf{n}}_W \cdot \nabla\phi|_{x_W} = 0 \tag{2.11}$$

As we discussed in Chapter 1.5, the majority of previous studies used a geometric formula (Ding and Spelt, 2007) or an approximation of the minimization of the free-energy functional to impose the wetting boundary condition. These methods may induce large parasitic currents or spurious velocities, or limit it only to the flat walls where the normal vector to the surface aligns with the grid. The wetting boundary equation we adapted in our research, on the other hand, is more flexible and is consistent with the nature of the phase-field models (Jacqmin, 1999) (Jacqmin, 2000).

2.2 Lattice Boltzmann Formulation

In this study, the diffuse interface lattice Boltzmann method (LBM) proposed by (Mitchell et al., 2018) is used to perform the multiphase simulation governed by the system (2.1). Two particle distribution functions f_i and g_i are used to resolve hydrodynamic equations and interface capturing equation, respectively. In the system, particles are allowed to move through collision and streaming processes. After each time step, the particle distribution is updated, which allows for direct calculation of the macroscopic fluid parameters in the system. The lattice structure is considered as a uniform grid. We scale the lattice spacing δx and time step δt as $\delta x = \delta t = 1$, and, thus, $c = \delta x/\delta t = 1$.

The lattice Boltzmann formulation to recover the governing equations are defined as

$$f_\alpha(\mathbf{x} + \mathbf{e}_\alpha \delta t, t + \delta t) = f_\alpha(\mathbf{x}, t) - \mathbf{M}^{-1}\hat{S}\mathbf{M}\left[f_\alpha(\mathbf{x}, t) - \bar{f}_\alpha{}^{eq}\right] + F_\alpha(\mathbf{x}, t) \tag{2.12a}$$

$$g_\alpha(\mathbf{x} + \mathbf{e}_\alpha \delta t, \mathbf{t} + \delta t) = g_\alpha(\mathbf{x}, t) - \frac{g_\alpha(\mathbf{x}, t) - \bar{g}_\alpha^{eq}(\mathbf{x}, t)}{\tau_\phi + 1/2} + F_\alpha^\phi(\mathbf{x}, t) \tag{2.12b}$$

Eq.(2.12a) is a velocity-based LBE to capture the hydrodynamics. It is an improved form of the velocity-based LB approach by Zu and He (Zu and He, 2013). The recovery of hydrodynamics equation is achieved by lattice population f_i using D3Q27 model. The D3Q27 model helps to improve the isotropy and increase the model accuracy. As shown in Fig.2.2(a), the weights ω_α^f and velocity direction e_α^f sets are defined as

$$\omega_\alpha^f = \begin{cases} \frac{64}{216}, & \alpha = 0 \\ \frac{16}{216}, & \alpha = 1 - 6 \\ \frac{1}{216}, & \alpha = 7 - 14 \\ \frac{4}{216}, & \alpha = 15 - 26 \end{cases} \tag{2.13}$$

$$e_\alpha^f = \begin{pmatrix} 0 & 1 & -1 & 0 & 0 & 0 & 0 & 1 & -1 & 1 & -1 & 1 & -1 & 1 & -1 \\ 0 & 0 & 0 & 1 & -1 & 0 & 0 & 1 & 1 & -1 & -1 & 1 & 1 & -1 & -1 \\ 0 & 0 & 0 & 0 & 0 & 1 & -1 & 1 & 1 & 1 & 1 & -1 & -1 & -1 & -1 \\ 1 & -1 & 1 & -1 & 1 & -1 & 1 & -1 & 0 & 0 & 0 & 0 & & & \\ 1 & 1 & -1 & -1 & 0 & 0 & 0 & 0 & 1 & -1 & 1 & -1 & & & \\ 0 & 0 & 0 & 0 & 1 & 1 & -1 & -1 & 1 & 1 & -1 & -1 & & & \end{pmatrix}$$

Eq.(2.12b) recovers the conservative phase-field equation by lattice population g_i. D3Q15 model is used in this case. Its applicability has been studied in (Fakhari et al., 2016a). This scheme is sufficient for modelling the phase-field equation as it allows the resolution of the zeros- and first moments of the distribution. As shown in Fig.2.2(b), the weights ω_α^g and velocity direction sets e_α^g for D3Q15 model are shown as

$$\omega_\alpha^g = \begin{cases} \frac{16}{72}, & \alpha = 0 \\ \frac{8}{72}, & \alpha = 1-6 \\ \frac{1}{72}, & \alpha = 7-14 \end{cases} \tag{2.14}$$

$$e_\alpha^g = \begin{pmatrix} 0 & 1 & -1 & 0 & 0 & 0 & 0 & 1 & -1 & 1 & -1 & 1 & -1 & 1 & -1 \\ 0 & 0 & 0 & 1 & -1 & 0 & 0 & 1 & 1 & -1 & -1 & 1 & 1 & -1 & -1 \\ 0 & 0 & 0 & 0 & 0 & 1 & -1 & 1 & 1 & 1 & 1 & -1 & -1 & -1 & -1 \end{pmatrix}$$

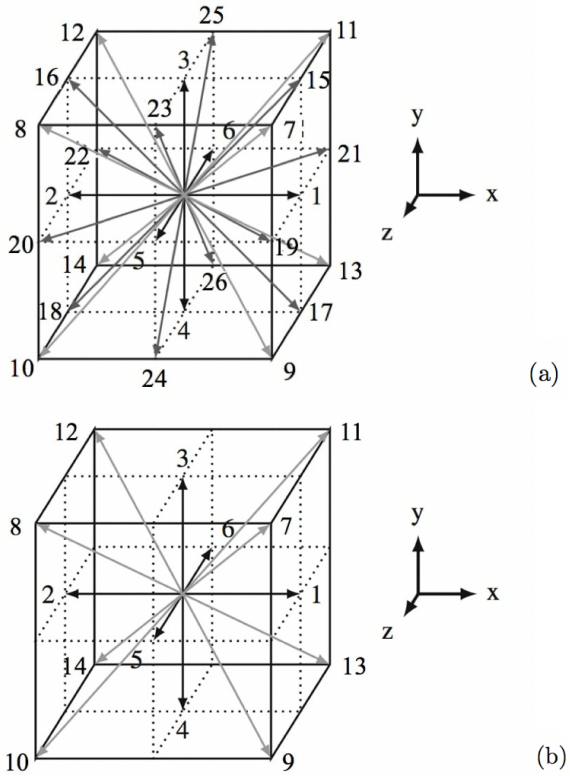

Figure 2.2: Lattice structure for the lattice Boltzmann formulation: (a) D3Q27 model, (b) D3Q15 model

Coupled with this eq.(2.12a), a weighed multiple-relaxation-time (WMRT) collision model (Fakhari et al., 2017a) was used to describe the collision operator, allowing the model to have the potential to achieve relatively large viscosity contrasts and simulate high Reynolds numbers.

The modified equilibrium distribution function $\bar{f_\alpha}^{eq}$ in eq.(2.12a) is calculated as

$$\bar{f_\alpha}^{eq} = f_\alpha^{eq} - \frac{1}{2}F_\alpha \tag{2.15}$$

with

$$f_\alpha^{eq} = \omega_\alpha^f \left[p^* + \left(\frac{e_\alpha^f \cdot \mathbf{u}}{c_s^2} + \frac{e_\alpha^f \cdot \mathbf{u})^2}{2c_s^4} - \frac{\mathbf{u} \cdot \mathbf{u}}{2c_s^2} \right) \right] \tag{2.16}$$

where p^* is the normalized pressure calculated as

$$p^* = p/c_s^2\rho \tag{2.17}$$

c_s is the speed of sound of the system, defined as $c_s = c/\sqrt{3}$.

Here, the modified equilibrium distribution function in eq.(2.15) is defined by subtracting half of the forcing term (according to trapezoidal rule or Crank-Nicholson discretization) from the regular equilibrium distribution function to simplify the collision step (Fakhari et al., 2017b).

In eq.(2.12a), the collision operator is adapted from WMRT scheme as (Fakhari et al., 2017a)

$$\Omega_\alpha = -\mathbf{M}^{-1}\hat{S}\mathbf{M}\left(f_\alpha(\mathbf{x},t) - \bar{f_\alpha}^{eq}\right) \tag{2.18}$$

where the orthogonal transformation matrix $\mathbf{M}$ is used to transfor the distribution functions from physical space into moment space and is given in Appendix A. The diagonal relaxation matrix is

$$\hat{\mathbf{S}} = diag(1,1,1,1,s_\nu,s_\nu,s_\nu,s_\nu,1,...,1) \tag{2.19}$$

The relaxation parameter s_ν relates to the hydrodynamic time τ by $s_\nu = 1/(\tau + 0.5)$ and the viscosity is set as $\mu = \rho\nu = \rho\tau c_s^2$, where ν is the bulk kinematic viscosity, μ and ρ is the bulk dynamic viscosity and density, respectively. Relaxation time τ is calculated by

$$\tau = \tau_L + \phi(\tau_H - \tau_L) \tag{2.20}$$

where τ_L and τ_H are the bulk relaxation times in the light and heavy fluids, and ϕ is the order parameter.

The hydrodynamics forcing term $F_\alpha(\mathbf{x},t)$ in eq (2.12a) is given by

$$F_\alpha(\mathbf{x},t) = \omega_\alpha^f \frac{e_\alpha^f \cdot \mathbf{F}}{\rho c_s^2} \tag{2.21}$$

where the forcing term is

$$\mathbf{F} = \mathbf{F}_s + \mathbf{F}_b + \mathbf{F}_p + \mathbf{F}_\mu \tag{2.22}$$

The surface force $\mathbf{F}_s$ and the body force $\mathbf{F}_b$ are calculated from the eq.(2.2) and eq.(2.4), respectively. The pressure force $\mathbf{F}_p$ and the viscous force $\mathbf{F}_\mu$ are introduced as a result of the recovery of the term $[\nabla\mathbf{u}+(\nabla\mathbf{u})^{\mathrm{T}}]$ in the velocity-based formulation in eq.(2.1b) (Zu and He, 2013). The pressure force $\mathbf{F}_p$ can be determined as (Fakhari et al., 2017b)

$$\mathbf{F}_p = -p^* c_s^2(\rho_H - \rho_L) \bigtriangledown \phi \tag{2.23}$$

and the viscous force $\mathbf{F}_\mu$ is (Fakhari et al., 2017b)

$$\mathbf{F}_\mu = \nu(\rho_H - \rho_L)\left[\bigtriangledown\mathbf{u} + (\bigtriangledown\mathbf{u})^T\right] \cdot \bigtriangledown\phi \tag{2.24}$$

where ρ_L and ρ_H are the densities of the light and heavy fluids, respectively, and the derivative of velocity is recovered from the second moment of the hydrodynamic distribution function as

$$F_{\mu,\beta} = -\frac{\nu(\rho_H - \rho_L)}{C_s^2}\left[\sum_\alpha e_{f\alpha,\beta} e_{f\alpha,\gamma} \sum_j (\mathbf{M}^{-1}\hat{S}\mathbf{M})_{i,j}(f_i - f_i^{eq})\right]\partial_\beta\phi \tag{2.25}$$

Macroscopic properties are recovered from the hydrodynamic distribution function as:

$$p^* = \sum_\alpha f_\alpha \tag{2.26}$$

$$\mathbf{u} = \sum_\alpha f_\alpha e_\alpha^f + \frac{\mathbf{F}}{2\rho} \tag{2.27}$$

In eq.(2.12b), the single-relaxation-time operator (BGK) is applied as collision operator, where $\tau_\phi = M/{c_s}^2$, and M is the Mobility.

The forcing term F_α^ϕ is defined as

$$F_\alpha^\phi(\mathbf{x}, t) = \delta t \frac{4\phi(1-\phi)}{\xi} \omega_\alpha^g e_\alpha^g \cdot \hat{\mathbf{n}} \tag{2.28}$$

The term $\bar{g}_i^{eq}$ suggests that the equilibrium distribution is shifted by the forcing term

$$\bar{g}_\alpha^{eq}(\mathbf{x}, t) = g_\alpha^{eq} - \frac{1}{2} F_\alpha^\phi \tag{2.29}$$

where

$$g_\alpha^{eq} = \phi \omega_\alpha^g \left(1 + \frac{e_\alpha^g \cdot \mathbf{u}}{c_s^2} + \frac{e_\alpha^g \cdot \mathbf{u}^2}{2c_s^4} - \frac{\mathbf{u} \cdot \mathbf{u}}{2c_s^2} \right) \tag{2.30}$$

The distribution function g_i can be related to the order parameter ϕ and ρ as

$$\phi = \sum_\alpha g_\alpha \tag{2.31a}$$

$$\rho = \rho_L + \phi(\rho_H - \rho_L) \tag{2.31b}$$

The gradient and Laplacian of the phase-field variable in the calculation of eq.(2.23) and eq.(2.24) are determined using second-order, isotropic centred differences, and then execute the dot product (Kumar, 2004) (Ramadugu et al., 2013), here we use the calculation under D3Q15 model as an example:

$$\bigtriangledown \phi = \frac{c}{c_s^2 \delta x} \sum_{\alpha=0}^{26} e_\alpha^g \omega_\alpha^g \phi(\mathbf{x} + e_\alpha^g \delta t, t) \tag{2.32}$$

$$\bigtriangledown^2 \phi = \frac{2c^2}{c_s^2 (\delta x)^2} \sum_{i=0}^{26} \omega_\alpha^g \left[\phi(\mathbf{x} + e_\alpha^g \delta t, t) - \phi(\mathbf{x}, t) \right] \tag{2.33}$$

For D3Q27 model, the implementation for eq (2.33) can be considered as (Thampi et al., 2013):

$$\bigtriangledown^2 \phi = \frac{1}{36} \left[16 \sum_{i=1}^{6} \phi_i^{(1)} + 4 \sum_{i=1}^{12} \phi_i^{(2)} + \sum_{i=1}^{8} \phi_i^{(3)} - 152 \phi^{(0)} \right] \tag{2.34}$$

where $\phi_i^{(1)}$, $\phi_i^{(2)}$ and $\phi_i^{(3)}$ stand for the nearest, second-nearest and third-nearest points nearby.

Notice that since different lattice structures are used for hydrodynamics and interface-capturing, the ω_α^g and e_α^g in eq.(2.32) and eq.(2.33) should be changed to

ω_α^f and e_α^f when calculating the surface tension force in eq.(2.2).

It is worthwhile to talk about the differences between the presented scheme and the one proposed by Zu and He (Zu and He, 2013), in order to highlight some advantages of the applied model. Besides using a Cahn-Hilliard model to capture the interface while we used a conservative phase-field model, there are also some differences in the calculation of hydrodynamics. First, Zu and He used finite difference scheme to calculate the forcing term in eq.(2.24). This adds another nonlocal variable to the system and, thus, impedes the efficiency of parallelization. In our scheme, the only nonlocal variable is the order parameter ϕ. The second difference is the way the equilibrium distribution function is calculated in eq.(2.15). We subtracted half of the forcing term not only to simplify the collision step, but to calculate all the equilibrium particle distributions at the same way. Zu and He distinguished the particle distribution function at rest ($\alpha = 0$) with other directions, which increased the calculation and was not physical in reality. The third difference is that the velocity and pressured was coupled in (Zu and He, 2013). A predictor-corrector scheme is needed to update the bulk pressure and velocity at each time step. While in our method, the velocity and pressure are updated separately through eq.(2.27) and eq.(2.26), so there is no need for a predictor-corrector scheme. We only need to make sure that the velocity is updated after the pressure.

2.3 Boundary Conditions for LBM

When applying numerical simulation in a finite domain, the boundary treatment is crucial. There are three different boundary conditions (BCs) used in our simulation: the periodic BC, the bounce back BC, and the wetting BC. Periodic BC is used to create a repeating flow pattern with a cyclic flow system, such that a large flow field can be approximated by a repeating smaller flow field. Bounce back BC is one of the most prevalent BCs to achieve the no-slip BC on liquid-solid interface. The explanation and two-dimensional application for periodic BC and bounce back BC using D2Q9 model is provided in Appendix B.

For this section, we focus on the implementation of the wetting boundary condition. Fakhari and Bolster proposed a way to implement wetting BC in two-dimensional cases using diffuse interface LBM in (Fakhari and Bolster, 2017). We adapted this scheme and expand it to the three-dimensional applications.

We cut a slice to the three dimensional simulation domain, as shown in Fig. 2.3. The blue nodes stand for the fluid nodes and the black nodes stand for the solid nodes.

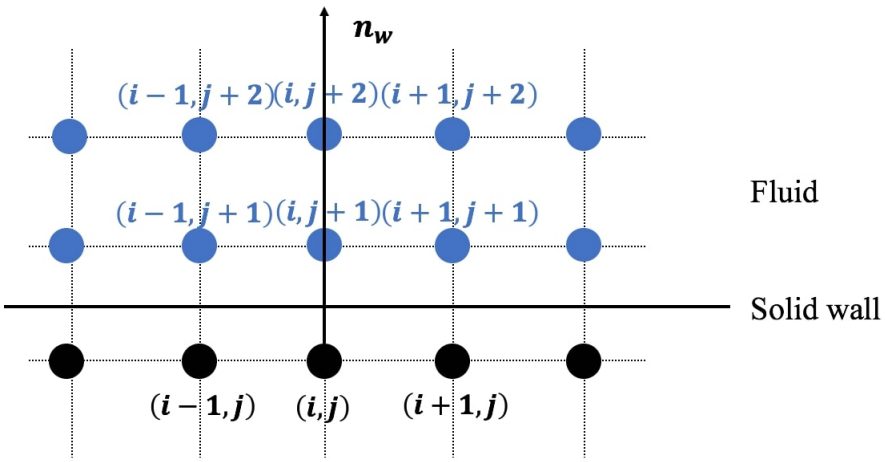

Figure 2.3: Node distribution on a two-dimensional lattice scheme, blue dots are the fluid nodes and black nodes are the solid nodes.

Recall the general wetting boundary condition in eq.(2.35):

$$\hat{\mathbf{n}}_W \cdot \nabla\phi|_{x_W} = \Theta\phi_W(1-\phi_W) \tag{2.35}$$

The left hand side of eq.(2.35) stands for the change rate of the phase field along the vertical direction at the wall. After applying central difference scheme based on

the node distribution in Fig 2.3, the left hand side can be written as

$$\hat{\mathbf{n}}_W \cdot \nabla\phi|_{x_W} = \left.\frac{\partial\phi}{\partial n_W}\right|_{x_W} = \frac{\phi_{i,j+1} - \phi_{i,j}}{2h} \tag{2.36}$$

where $h = |x_{i,j+1} - x_w|$ and $h = 0.5$ in our case because we use a halfway bounce back boundary condition and, thus, the wall should stay between the centers of the two adjacent nodes.

The term ϕ_W on the right hand side of eq.(2.35) can be approximated as $\phi_W = (\phi_{i,j+1} + \phi_{i,j})/2$. Combined with eq. (2.36), eq.(2.35) can be rewritten as

$$\frac{\phi_{i,j+1} - \phi_{i,j}}{2h} = \Theta\frac{\phi_{i,j+1} + \phi_{i,j}}{2}(1 - \frac{\phi_{i,j+1} + \phi i, j}{2}) \tag{2.37}$$

The quadratic equation gives us a solution as

$$\phi_{i,j} = \frac{1}{a}\left(1 + a - \sqrt{(1+a)^2 - 4a\phi_{i,j+1}}\right) - \phi_{i,j+1} \tag{2.38}$$

where $a = h\Theta$.

In our case, $\phi_{i,j+1}$ value can be adapted from the previous time step in the iteration since the phase-field is not expected to change rapidly in our system.

For the neutral wetting boundary condition, eq. (2.11) has a simple solution as

$$\phi_{i,j} = \phi_{i,j+1} \tag{2.39}$$

Eq.(2.38) and eq.(2.39) give us the relationship of the ϕ field value between the nodes inside the solid wall and the nodes outside the solid wall. The coefficient a is related to the contact angle θ. The gradients and Laplacian at the solid wall can, thus, be calculated by eq.(2.32) and eq.(2.33) and then the information can be passed back to the entire system through the particle collision and streaming processes, allowing the system to self-develop to the contact angle θ we specified.

Since the implementation of the wetting BC is not applied using a geometric formula or an approximation form of the free-energy function, it can also be implemented to the curved surfaces (Fakhari and Bolster, 2017). We only focus on its implementation at the flat surfaces.

2.4 Solution Algorithm

As briefly stated before, the update of the distribution functions f_α and g_α are achieved through the collision and streaming processes. The solution algorithm is explained on one population distribution g_α for simplicity.

Recall eq.(2.12b) to capture the interface

$$g_\alpha(\mathbf{x}+\mathbf{e}_\alpha\delta t, \mathbf{t}+\delta t) = g_\alpha(\mathbf{x},t) - \frac{g_\alpha(\mathbf{x},t)-\bar{g}_\alpha^{eq}(\mathbf{x},t)}{\tau_\phi+1/2} + F_\alpha^\phi(\mathbf{x},t) \tag{2.40}$$

We can decompose this equation into two distinct parts that are performed in succession:

1. The first part is collision

$$g_\alpha^\star(\mathbf{x},t) = g_\alpha(\mathbf{x},t) - \frac{g_\alpha(\mathbf{x},t)-\bar{g}_\alpha^{eq}(\mathbf{x},t)}{\tau_\phi+1/2} + F_\alpha^\phi(\mathbf{x},t) \tag{2.41}$$

where $g_\alpha^\star$ represents the distribution function after collision.

2. The second part is streaming (or propagation)

$$g_\alpha(\mathbf{x}+\mathbf{e}_\alpha\delta t, \mathbf{t}+\delta t) = g_\alpha^\star(\mathbf{x},t) \tag{2.42}$$

The LBE is consisted of two parts: collision and streaming. The collision is simply an algebraic local operation. First, we calculate the density ρ, the macroscopic velocity $\mathbf{u}$ and the forcing term F_α^ϕ to find the modified equilibrium distributions term $\bar{g}_\alpha^{eq}(\mathbf{x},t)$ as in eq.(2.12b) and the post-collision distribution $g_\alpha^\star(\mathbf{x},t)$ as in eq.(2.41). After collision, we stream the resulting distribution $g_\alpha^\star(\mathbf{x},t)$ to neighbouring nodes as in eq.(2.42. When these two operations are complete, one time step is finished, and the operations are repeated.

Fig.2.4 shows a typical process of particle's streaming and collision.

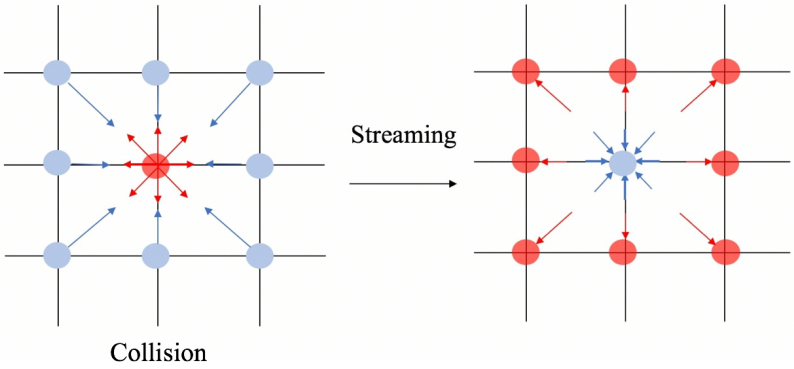

Figure 2.4: Paricle streaming and collision processes

In Fig.2.4, red particles are streamed from the central node to its neighbours, while blue particles are streamed back. Left image shows the post-collision distributions $g_\alpha^\star$ and right figure gave us pre-collision distributions g_α after streaming.

In our LBM based on diffuse-interface phase-field method, the calculation algorithm is complex, especially when the boundary conditions come into play. Here we give a detailed description about the solution algorithm to show our calculation sequence and the update of variables.

1. Initialization:

(1) Initialize variables: normally we initialize our velocity field as $\mathbf{u} = 0$, phase-field as $\phi = 1$ for the heavy fluid and $\phi = 0$ for the light fluid, and pressure field as $p = 1$. Density field can be generated from eq.(2.31b) and normalised pressure p^* can be generated from eq.(2.17).

(2) Initialize distribution functions: first, we calculate gradients and Laplacians of ϕ through eq.(2.32) and eq.(2.33). The chemical potential μ_ϕ, normal vector $\mathbf{n}$, and forcing term F can be calculated accordingly from eq.(2.3), eq.(2.5) and eq.(2.22). The hydrodynamic forcing for distribution f_α and g_α is calculated as eq.(2.21) and eq.(2.28). The terms f^{eq}, $\bar{f}_\alpha^{eq}$, g^{eq} and $\bar{g}_\alpha^{eq}$ are updated according to eq.(2.16), eq.(2.15), eq.(2.30) and eq.(2.29), respectively. The initialized equilibrium distributions are replaced by equilibrium values $\bar{f}_\alpha^{eq}$ and $\bar{g}_\alpha^{eq}$. Notice that since we use different lattice structures for hydrodynamics and interface-capturing, the gradients and Laplacians need to be calculated and stored separately. When applying them, use the ones from D3Q27 model for all variables related to f_α and use the ones from D3Q15 for all variables related to g_α.

2. Collision:

Since we have updated the variables in step 2, hydrodynamic forcing and equilibrium distribution functions need to be updated too, as shown before. The collision operator Ω_α is calculated from eq.(2.18), together with the diagonal relaxation matrix from eq.(2.19) and relaxation time from eq.(2.20). f_α is updated through WMRT scheme as shown in eq.(2.12a), and g_α is updated through BGK scheme as shown in eq.(2.12b).

3. Streaming:

f_α and g_α is streaming everywhere in the system, as the example presented in eq.(2.42). Bounce-back boundary condition is also applied in where there is a solid

wall. The detailed explanation for bounce-back boundary condition is presented in Appendix B.

4. Update the macroscopic variables:
(1) Variables ρ and ϕ are updated from distribution function f_α and g_α through eq.(2.31a) and eq.(2.31b). Wetting boundary conditions is applied to update the nodes near the solid wall as eq.(3.9)
(2) We repeat the calculation for gradients and chemical potential as introduced in step 1.(2), to calculate surface forcing F_s and forcing term from F from eq.(2.2) and eq.(2.22). The variables p^* and $\mathbf{u}$ then can be updated from eq.(2.17) and eq.(2.27), note that velocity is updated after the normalised pressure.

5. Update time step:
Increase the time step, setting t to $t + \Delta t$, and go back to step 2 until the last time step or convergence has been reached.

6. Data output

In order to give a straightforward description, we also present an overview of one cycle of our applied LB algorithm. As shown in Fig. 2.5, our LBM algorithm is consisted of a cyclic sequence of sub-steps, with each cycle corresponding to one time step. Notice that only main sub-steps are shown in the figure to keep it simple.

The internal order of these sub-steps is important, because later steps depend on the results of earlier steps. Through continuous streaming and collision, the distribution functions are continuously updated, as well as the macroscopic parameters, until the entire system reaches an equilibrium state where there is no apparent changes between the time steps.

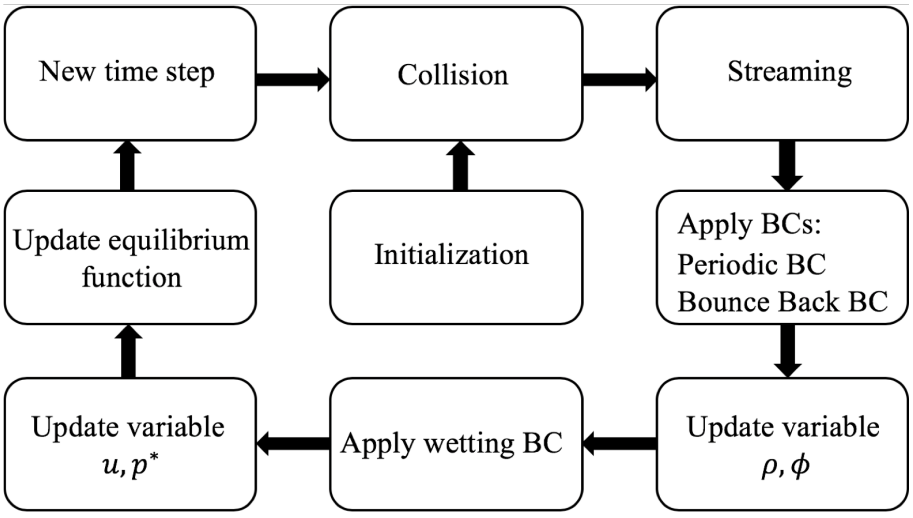

Figure 2.5: An overview of one cycle of the applied LB algorithm

2.5 Parallelization

Parallelization of the code is a crucial part of improving the efficiency of the simulations. In our research, we used message-passing interface (MPI) (Gropp et al., 1999) for parallelization.

In our simulation, we divide the entire domain into several equal-sized sub-domains. Each CPU is assigned one sub-domain. A receive-sent scheme is applied for the communication between the sub-domains, and command MPI_SENDRECV is used. to Recall that the only non-local variable in the formulation is the order parameter ϕ.

In our case, we only do parallelization for the z direction, not in x or y directions. In Fig. 2.6, k represents the location in z direction and other two directions will be written as x and y. We divide the entire domain into three sub-domains and each domain length is $(k_{end} - k_{sta})$. When doing calculation for each domain, we add an additional layer to both sides of the parallelized direction. These additional layers are used to receive the ϕ value from the next sub-domain. Therefore, we have

$$\phi(i, j, ksta - 1) = \phi(i, j, kend) \tag{2.43a}$$

$$\phi(i, j, end + 1) = \phi(i, j, ksta) \tag{2.43b}$$

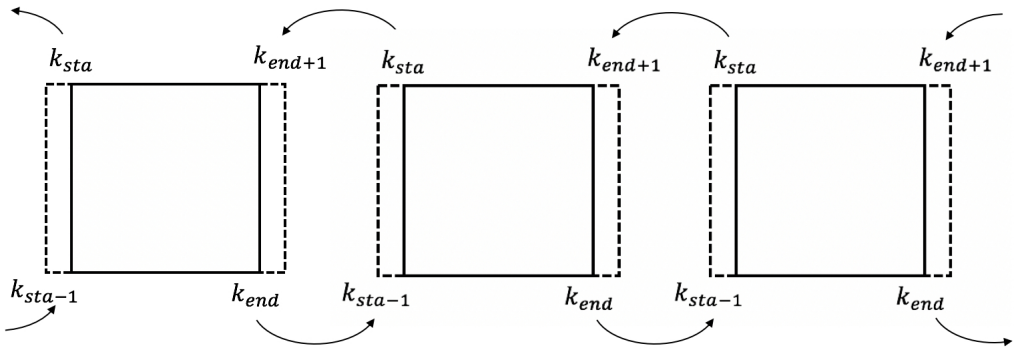

Figure 2.6: Sub-domains used for parallelization and variables exchange

We apply command MPI_SENDRECV only before the update of the gradients or Laplcians (in step 2.(2)).

Parallelization significantly reduces the simulation time, and allows us to consider larger domain in order to obtain accurate results.

Chapter 3

Drop Behavior on a Solid Surface

In this chapter, the capability of the conservative phase-field lattice Boltzmann method to capture the static contact angle is validated: a semi-circular drop is placed on a solid surface and let to equilibrate. In the following sections, we introduce the physical background of this process: what happens intermolecularly and what contributes to the final equilibrated shape of the drop. The simulation is performed, and the equilibrium contact angle is measured and compared to the theoretical value. The focus is given to numerical implementation of the wetting boundary conditions.

3.1 Physical Background

If a liquid droplet is placed on a solid surface, it will reach an equilibrium state with the surrounding phase and form a contact angle with the solid surface. The equilibrium shape of the drop placed on the solid surface depends on certain properties of the system. In this section, we explain the physics behind the surface wetting phenomenon and identify the parameters that describe the system.

3.1.1 Surface Tension

Surface tension has the tendency of the fluid surfaces to shrink into the possible minimum surface area (De Gennes et al., 2013). In microscopic view, a liquid is a condensed state in which molecules attract each other (Graf et al., 2006). When the molecular attraction is stronger than the thermal motion, molecules will change from gas phase to liquid phase. Typically, the molecules inside the liquid volume feel the cohesive forces from the neighbouring molecules and all the forces result in

a net force of zero. However, the molecules at the surface boundary only feel the cohesive forces from one side of the neighbouring molecules and, therefore, have the tendency to be pulled inside. This leads to internal pressure and forces the surface to minimise its area, resulting in a spherical surface (De Gennes et al., 2013).

Another way to view the surface tension is in terms of energy. A molecule in contact with a neighbour is in a low energy state, comparing to when it is not in the contact. Therefore, the molecules inside the liquid volume are of low energy state, while the ones at the surface boundary are of comparably high energy state. In order to minimize the energy of the system, the number of high-energy molecules has to be minimized, which results in a minimization of the drop surface area (De Gennes et al., 2013).

At liquid–air interfaces, surface tension results from the greater attraction of liquid molecules to each other (due to cohesion) than to the molecules in the air (due to adhesion). The net effect is an inward force at its surface that causes the liquid to behave as if its surface were covered with a stretched elastic membrane. Thus, the surface comes under tension from the imbalanced forces, which is probably where the term "surface tension" came from. The surface energy between the two phases liquid L and gas G is normally characterized by an interfacial tension σ_{LS}, which is an important parameter in determining the shape of the liquid drop in such system.

Although the surface tension σ can be explained at the molecular level, it is a macroscopic parameter defined on a macroscopic scale (De Gennes et al., 2013). Physically, surface tension can have the dimension of energy per area or force per length. On the one hand, creating surfaces needs energy supply. Suppose one wants to increase the surface area of a liquid drop by an amount of dA, the corresponding number of liquid molecules have to be brought to the surface boundary of the liquid volume and we can write the energy needed as

$$\delta W = \sigma \cdot dA \tag{3.1}$$

where σ is the interfacial tension and δW is the needed energy. Dimensionally, $[\sigma] = EL^{-2}$. The unit is expressed as mJ/m^2. In other words, σ is the needed energy to increase the surface area by one unit.

Surface tension also contributes to thermodynamic work. It can be defined as the increase in free energy F with the an increase in surface area:

$$\sigma = \left[\frac{\partial F}{\partial A}\right]_{T,V,n} \tag{3.2}$$

where n is the number of molecules and V is the total volume.

On the other hand, surface tension can be viewed as a force per length. This can be easily observed in many experiments. One of the most famous experiment is the liquid membrane supported by a rigid frame experiment introduced in (Wick, 1997). It illustrates how much work is needed to increase a certain amount of the surface area and how it relates to the interfacial tension of the system. As shown in Fig 3.1, a flexible loop, secured by two threads to the frame, is embedded in the membrane. Without any forces applying, the rob has the tendency to move left so as to minimize the surface area. Therefore if the rob moves a distance dx (to the right), the needed energy can be written as

$$\delta W = F \cdot dx = 2\sigma \cdot l \cdot dx \tag{3.3}$$

where the factor 2 reflects the presence of two interfaces of the system. In conclusion, $\vec{\sigma}$ is can be viewed as a force per unit length to the rod in the plane of the surface and directed towards the liquid.

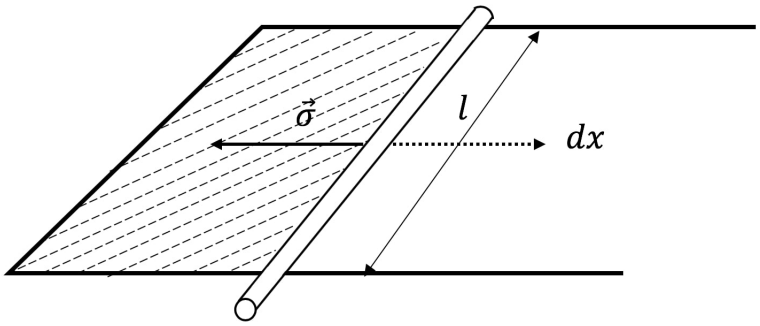

Figure 3.1: Experiment of the measurement of surface tension, adapted from (Wick, 1997)

3.1.2 The Capillary Length

Surface tension is not the sole determinant for the shape of the liquid volume after being put on a solid surface. We also need to take gravity force into consideration. There exists a particular length- capillary length κ_{CL}, beyond which the gravity becomes important. It can be estimated by equating the Laplace pressure σ/κ_{CL} and hydrostatic pressure $\rho g \kappa_{CL}$. Where ρ is the density at a depth κ_{CL} and $g = 9.8m/s^2$

is the earth's gravity acceleration.

$$\kappa_{CL} = \sqrt{\frac{\sigma}{\rho g}} \tag{3.4}$$

As shown in Fig. 3.2, for small drops of radius less than κ_{CL}, the gravity force is negligible. The capillary forces are the only forces that come into play and the droplet forms a spherical cap after being placed on a solid surface. For larger drops, the gravity force becomes dominant, thus the top part of the droplet can be flattened. If the radius continues to increase, the drop might wet the whole surface and can no longer maintain any shape.

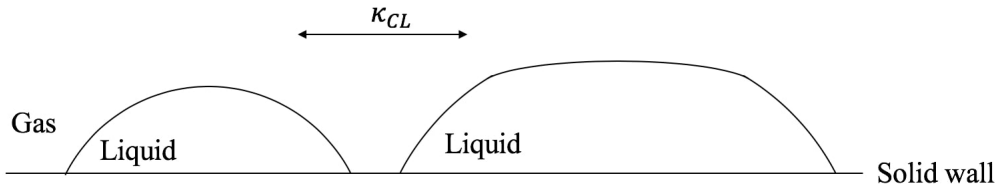

Figure 3.2: Gravity effect on droplet final shape

The order of the capillary length κ_{CL} is typically within millimetres. The cases we considered in our research are only for small drops for which the gravity force is negligible. Therefore in our case, the shape of the liquid volume remains a spherical cap after being placed on a solid wall.

3.2 Wetting and Contact Angle

When a liquid droplet is placed on a solid surface, it will stay in the shape of a spherical cap due to the existence of surface tension (we do not take gravity force into consideration due to the small drop size). The angle that the liquid surface makes with the solid support is described as the contact angle.

As shown in Fig 3.3 , the equilibrium force balance in the horizontal direction can be written as:

$$F_{LG} \cos\theta = F_{SG} - F_{SL} \tag{3.5}$$

where F_{LG}, F_{SG} and F_{SL} refer to the interface forces of liquid-gas surface, solid-gas surface and solid-liquid surface, respectively; θ is the contact angle.

This equation was proposed by Thomas Young in 1805. From the equation, it is clear that if the interfacial tension force of the solid-gas interface is larger than

the interfacial tension force of solid-liquid interface ($F_{SG} > F_{SL}$), the contact angle $\cos\theta$ has to be positive and θ is thus less than 90°, the liquid has the tendency to spread and partially wets the solid, the solid wall is then called the hydrophilic surface (Graf et al., 2006). If the solid-liquid interfacial tension force is larger than the solid-gas interfacial tension force ($F_{SL} > F_{SG}$), the contact angle will exceed 90° and the solid wall is thus called the hydrophobic surface. (Fakhari and Bolster, 2017) (See Fig 3.4).

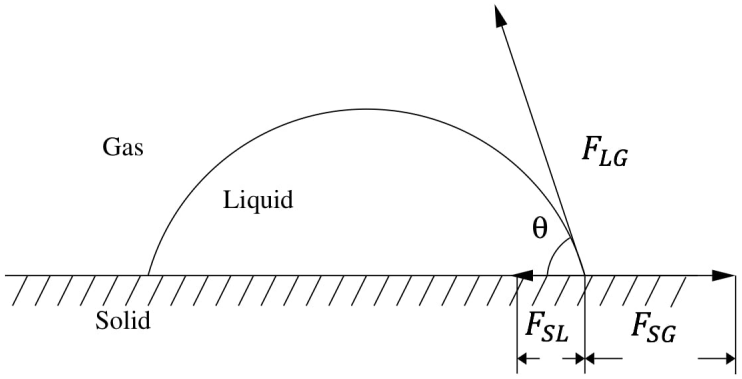

Figure 3.3: Force balance under equilibrium

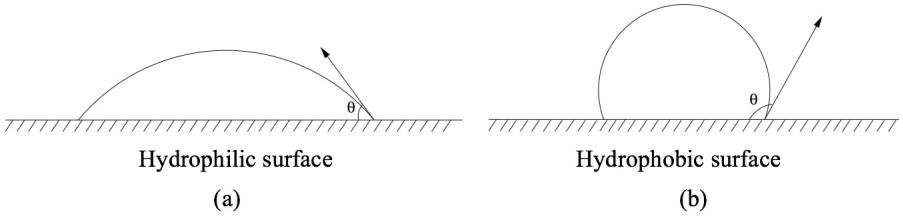

Figure 3.4: Hydrophilic surface (a) and hydrophobic surface (b)

Young's equation is the foundation of wetting phenomena study, but it is very difficult to be verified because the interface tension force measurement in reality is quite difficult (De Gennes et al., 2013). In addition to the challenges exposed by experiments, there are also some objections to the physical content of Young's equation (Hiemenz and Rajagopalan, 1997). The objections can be roughly classified into two categories: first, the Young's equation neglects the surface roughness and chemical heterogeneity for the actual solid phase (Hiemenz and Rajagopalan, 1997). Some researchers have added empirical corrections to the equation in order to solve

this problem. For example, if the surface is rough, the surface area where the liquid is in contact with the solid phase is actually larger than estimated. A term $\cos\theta$ is thus added to the left hand side of the eq. (3.5) to balance the projection of F_{LG} on the solid surface:

$$\cos\theta F_{LG}\cos\theta = F_{SG} - F_{SL} \tag{3.6}$$

where $\cos\theta > 1$, in order to make up for the underestimation of the surface area. For heterogeneous surface, we simply identify two different surfaces to be chemical type 1 and chemical type 2. Fraction f_1 and f_2 are assigned to be the percentage of chemical type S_1 and S_2. Eq.(3.5) can then be revised as

$$F_{LG}\cos\theta = f_1(F_{S_1V} - F_{S_1L}) + f_2(F_{S_2V} - F_{S_2L}) \tag{3.7}$$

where $f_1 + f_2 = 1$. Although corrections are made to the original Young's equation, the validations of both conditions are even harder than before. Therefore the accuracy of eq.(3.5) is continued to be questioned.

Another objection to the Young's equation is concentrated on whether the surface is in a true thermodynamic equilibrium state. The core problem towards this argument is whether the surface is thermodynamically the same as an ideal surface without such system being placed above. From Fig. 3.3, we can see that F_{LG} has a projection term on the solid surface: $F_{LG}\sin\theta$. On deformable solid surface, this term will produce a ridge to the surface. On harder solid surface, we are not sure if the term will cause a deformation of the surface. Clearly, only when $\theta = 0^\circ$ can the surface be in a true thermodynamic state.

Young's equation is very controversial during the past decades because it oversimplified several important factors in real physical process (Hiemenz and Rajagopalan, 1997). However, the fact that it placed a solid foundation to surface wetting research and its capability under ideal conditions analysis cannot be denied. It gives us a sense of how the wetting phenomena is related to the contact angle and the interface tension, which is exactly our starting point for this research.

Back to our case, when a semi-circular liquid drop is placed on a solid surface, due to the existence of the surface tension and certain solid surface characteristic, the drop will automatically deform and reach to an equilibruim state. Mathematically, the relationship between the maximum height of a droplet and its contact angle can be derived (Fakhari and Bolster, 2017) for the equilibrated system. As shown in Fig. 3.5, the mass per unit density of the droplet can be written as $A = r^2(\pi - \alpha + \sin\alpha\cos\alpha)$, where $\alpha = \pi - \theta$. Recall that the initial mass per unit density of the droplet is $A_0 = \pi R^2/2$. According to the mass conservation law, we have $A = A_0$.

Thus, we have

$$\frac{h_{max}}{R} = 1 - \cos\theta\sqrt{\frac{\pi}{2\theta - \sin 2\theta}} \tag{3.8}$$

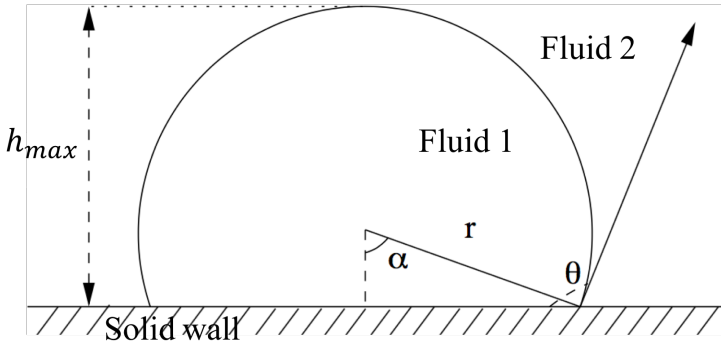

Figure 3.5: Contact angle θ and the maximum height h_{max} of a droplet

To validate that the adapted numerical model can capture the static contact angle, the following simulations cases were performed. First, a semi-circular droplet was placed on the solid surface, then the system of the governing equations was solved to reach the equilibrium state. Finally, the numerical simulation results of the maximum height of the drop and the contact angle was compared to the theoretical solution. The simulation was done with two fluid phases with equal density and equal viscosity.

3.3 Numerical Model and Parameters

In LB simulation, we use lattice unit (lu) to describe the length scale of numerical parameters. The simulation parameters were applied as: surface tension $\sigma = 0.01$, interface thickness $\xi = 3$ (lu) , $\tau_\phi = 1$, mobility $M = 1/3$, density ratio $\rho_H/\rho_L = 1$, viscosity ratio $\mu_H/\mu_L = 1$. The simulation domain size is of $nx \times ny \times nz = 90 \times 60 \times 40$ (lu), the initial drop was placed at $(nx/2, ny/2, 0)$, the initial diameter of the droplet is $36(lu)$. Periodic boundary condition was applied in x and y directions, halfway bounce back was used on the top boundary to replicate no-slip boundary condition, wetting boundary was applied to the bottom boundary.

3.4 Numerical Results

We tested four different non-neutral contact angles ($\theta = 30°, 60°, 120°$ and $150°$) and observed drop deformation process and final equilibrium state. The final equilibrium states for each case are presented in Fig 3.6.

To quantitatively assess the accuracy of the numerical results, the maximum equilibrium height of the drop obtained numerically was compared to the theoretical prediction given by eq (3.8). The comparison between the analytical and numerical results is shown in Fig 3.3. The maximum relative deviation is 3.3% and it is achieved at the contact angle of 120°.

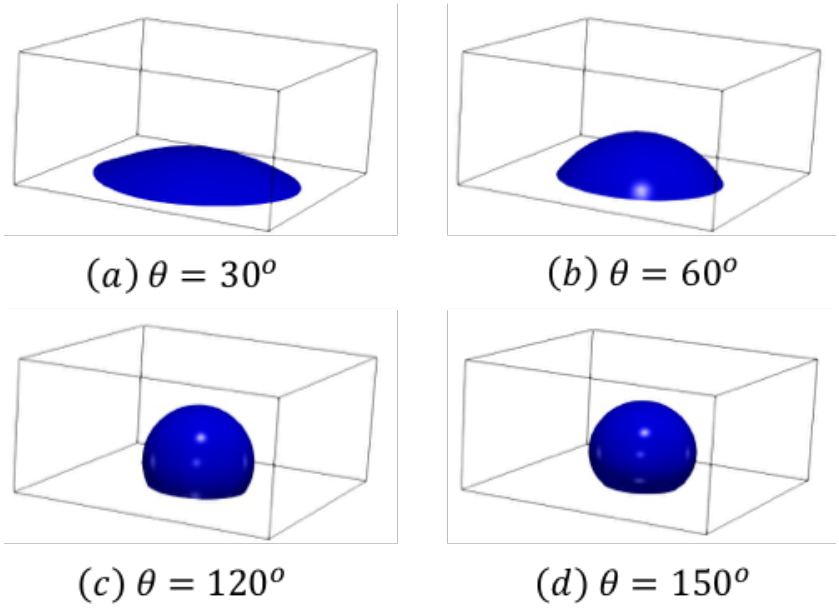

Figure 3.6: Equilibrium state of the drop with different contact angles

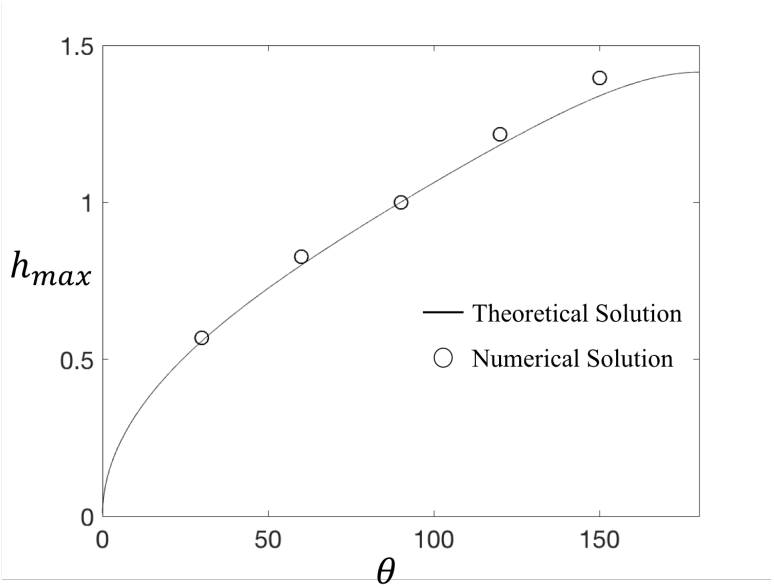

Figure 3.7: Comparison between analytical and numerical results for the maximum height of the drop, as a function of θ

3.5 Curve Fitting Method

In the previous section, we presented the equilibrium state of drops with different contact angles in Fig.3.6 and the comparison between analytical and numerical results in terms of the maximum of the drop height for each case in Fig.3.7. In order to get a further description about the accuracy of our method, we want to directly measure the equilibrium contact angles and compare them to the proposed contact angles when we initialize the simulation. This led us to consider the possible methods to calculate the contact angle. Several experimental methods to measure the contact angle are introduced in (Law and Zhao, 2016). Here, we chose to apply a curve fitting method to quantitatively identify the contact angle.

As shown in Fig 3.8, the dashed white curve is an arc that best fits the drop interface ($\phi = 0.5$). We plotted the whole simulation domain in Cartesian coordinates such that we can easily get the point of intersections of the drop interface and our x axis: (x_1, y_1) and (x_3, y_3). (x_2, y_2) is the position of our center of the fitted circle. The intersection angle θ_1 in Fig 3.8 then can be calculated directly from the above coordinates:

$$\theta_1 = \arccos\left[\frac{(x_3 - x_1, y_3 - y_1) \cdot (x_2 - x_1, y_2 - y_1)}{(|(x_3 - x_1, y_3 - y_1)| \cdot |(x_2 - x_1, y_2 - y_1)|)}\right] \tag{3.9}$$

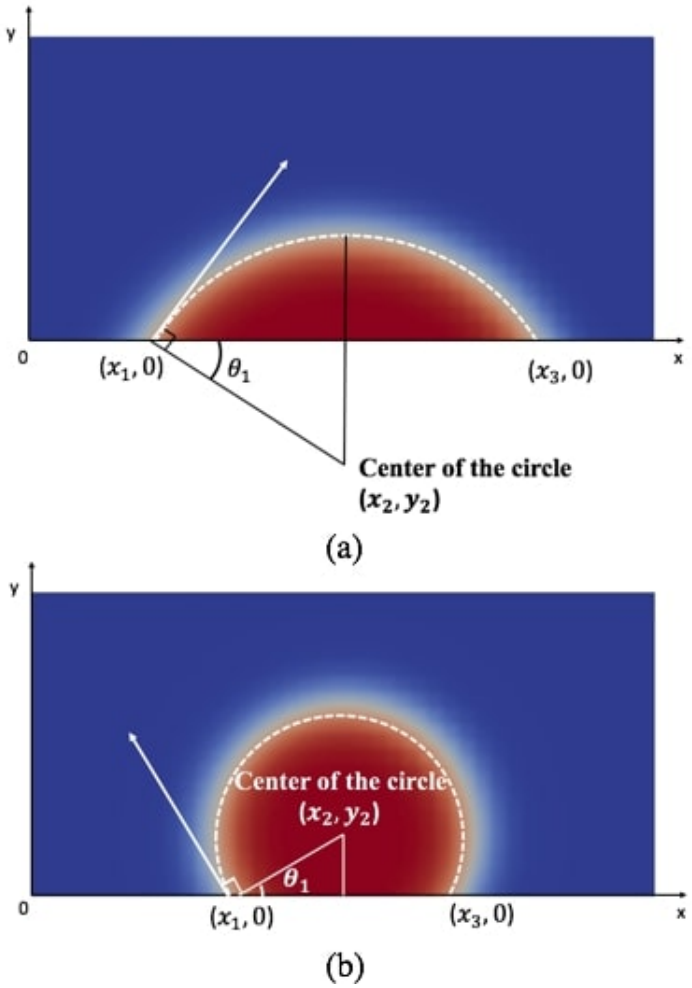

Figure 3.8: The curve fitting method for (a) hydrophilic surface and (b) hydrophobic surface

For a hydrophilic surface as shown in Fig.3.8 (a), the contact angle can be calculated as $\theta = 90° - \theta_1$ and for a hydrophobic surface as shown in Fig.3.8 (b), the contact angle is $\theta = 90° + \theta_1$. We used the curve fitting method to measure the contact angle for each case. The interface was halved into two to measure the left and right contact angle separately and the average is taken to minimize the calculation error. The measured contact angle for four cases are shown in Table 3.1. The largest deviation between measured contact angle and specified contact angle is 4.3%, achieved at $\theta = 30°$. All the contact angles were measured after the system came to an equilibrium state.

Table 3.1: List of measured contact angles for each simulation

Specified contact angle	*Measured contact angle*
30°	28.7°
60°	61.6°
90°	88.8°
120°	125.2°
150°	144.3°

3.6 Conclusions

In this chapter, we briefly went through the physical background of the proposed system and the surface wetting phenomenon. The capability of the current implementation of wetting boundary condition to capture the static contact angle was validated by putting a semi-circular drop on a solid surface and observed its final equilibrium state. We compared the differences between the numerical simulation results and analytical results in terms of both the maximum height of the drop and its equilibrated contact angle, the deviation was less than 6% and thus testified the model accuracy.

The possible reasons accounting for the differences between specified contact angle and measured contact angle include the existence of model error when we chose the numerical method, round-off error led by computer precision and errors that may appear when we applied the curve fitting method to measure the contact angle.

Chapter 4

Drop Sliding in a Simple Shear Flow

This chapter is devoted to the validation of the wetting boundary condition to capture the three-dimensional contact line motion. The cases were done by applying numerical studies of drop sliding cases between two parallel solid plates. In particular, we pay attention to its ability to capture the contact angle during the drop motion.

4.1 Background

Studying the three-phase contact line motion is of great importance, as it is widely encountered in many industrial applications and everyday life. Take multiphase flow in porous media as an example, it requires us to study the drop behavior in very confined channels and the dynamic interaction of the phases with each other and with the adjacent walls (Derksen, 2015).

In this chapter, motivated by the aim to elucidate the dynamic interaction between fluid phase and solid wall for flow in porous media, we use LBM simulations to study the drop behavior in a shearing flow, which requires an accurate capture of the three-phase contact line motion.

To validate the capability of the method to capture contact line motion, we simulated a single drop sliding in a simple shear flow. Similar simulations have been done before, but using different numerical methods: Derksen (Derksen, 2015) used molecular dynamic simulations to investigate contact line motion. In this study, a sessile drop of Fluid 1, immersed in Fluid 2 was placed on a solid surface, the then system was sheared. The specific focus was given to the relationship between the

dimensionless sliding speed of the drop of Fluid 1 and the contact angles of the drop on the substrate. Considering the limitation that molecular dynamic simulation can only handle microscopic system, another paper (Derksen and Komrakova, 2019) applied and tested the free-energy lattice Boltzmann method for the accuracy of three different wetting boundary conditions for the same cases.

4.2 Problem Statement

We consider a fluid system with two parallel solid plates. First, we placed a semi-circular droplet with a radius R_0 consisting of Fluid 1 on the bottom solid surface in the surrounding of Fluid 2, then let the system equilibrate to a specified angle. Both fluid have the equal density ρ and viscosity ν. After the equilibrium state was achieved, we generated a shear flow with shear rate G by moving the bottom and top solid wall with opposite velocity directions, which allowed the droplet to deform and move, as shown in Fig 4.1. θ_r and θ_a represented the receding and advancing contact angle respectively.

For a multiphase system, there are two important kinetic effects: hydrodynamic and thermodynamic, leading to a distinction between 'static' and 'dynamic' contact angles (Berg, 2010). Hydrodynamic analysis shows that viscous effect is primarily responsible for the dynamic wetting behavior, and it can be describe using the Capillary number Ca as

$$Ca = \frac{\mu V}{\sigma} \tag{4.1}$$

where μ is the dynamic viscosity of the liquid, V is a characteristic velocity and σ is the interfacial tension between the two fluid phases.

The capillary number is a dimensionless quantity, and is the ratio of viscous force and surface tension force term in the system. For low capillary numbers (normally less than 10^{-5}), flow is dominated by the capillary forces. Whereas for higher capillary number (more than 10^{-4}), the capillary forces are negligible compared to the viscous forces. The capillary number plays a key role in the dynamics of moving flow, in particular it governs the dynamic contact angle of a flowing droplet at an interface (Lambert, 2013).

Similarly, several dimensionless parameters were chosen to describe the drop shearing process for our LBM simulation: the capillary number $Ca = \rho\nu G R_0/\xi$, the Reynolds number $Re = G{R_0}^2/\nu$, the contact angle θ and the aspect ratio R_0/h with h the distance between two parallel solid plates. All the units conversion were referred to paper (Derksen and Komrakova, 2019).

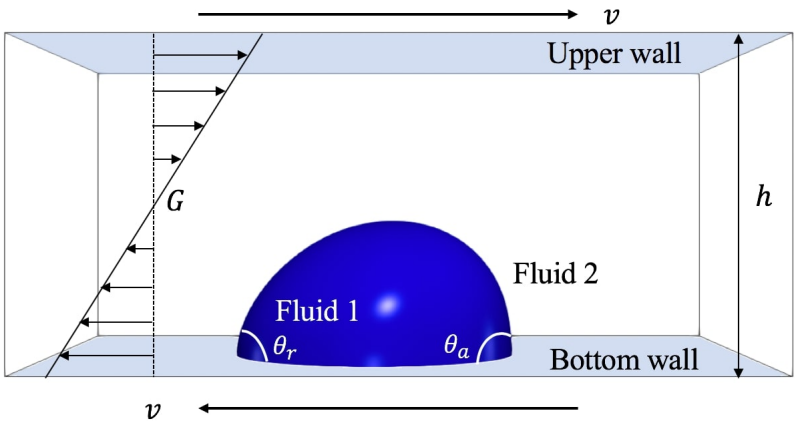

Figure 4.1: Droplet moving under shear rate G

4.3 Numerical Results

Here we keep $Ca = 0.16$ and $Re = 0.26$ in order to align with the cases introduced by (Derksen and Komrakova, 2019). The simulation domain size is designed as $nx \times ny \times nz = 90 \times 60 \times 40$, the shearing rate $G = 2.67 \cdot 10^{-4}$, the shearing velocity $v = 5.334 \cdot 10^{-3}(lu)$ for the top wall and $v = -5.334 \cdot 10^{-3}(lu)$ for the bottom wall. For the boundary treatment of the domain, the bottom and top walls were assigned with the wetting boundary condition and the left and right walls were assigned with the periodic boundary conditions, which allowed the droplet to leave and come back to the domain in horizontal directions.

In Fig 4.2, three cases with different initial wetting angles (65°, 90° and 111°) were performed. During the shearing process, the drop would deform and move with the bottom solid wall, then finally reach a terminal velocity.

The receding angle θ_r and the advancing angle θ_a for all three cases are measured after the droplet reached their terminal velocity. Fitting curve method introduced in chapter 3.4 was used to quantitatively measure the contact angles. Our lattice Boltzmann simulation results were compared to the molecular dynamics results presented by ((Derksen and Komrakova, 2019)) as shown in Fig 4.3.

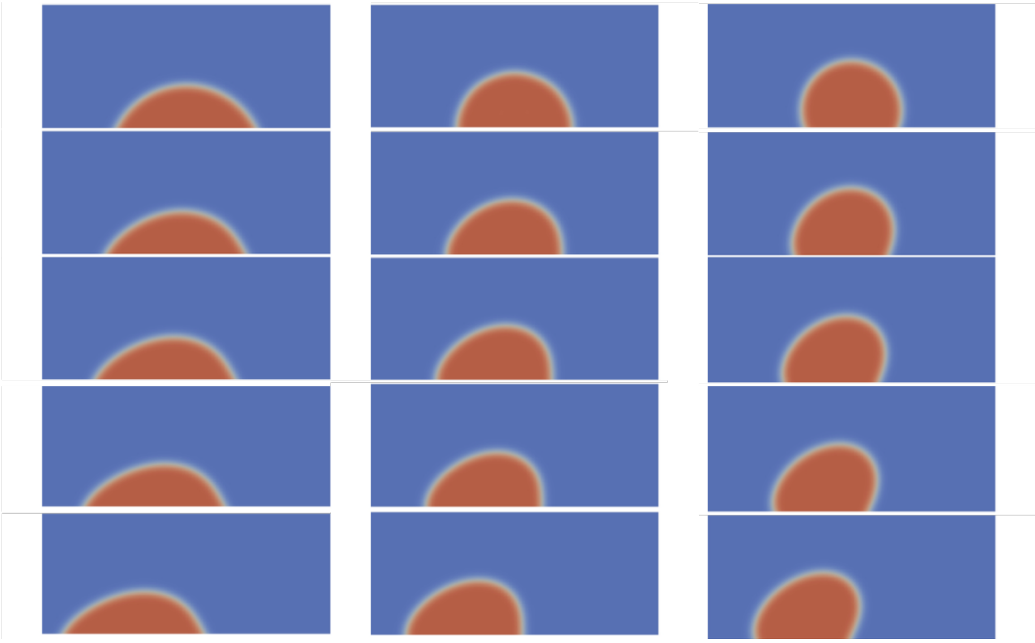

Figure 4.2: Drop deformation and movement for initial contact angle (from left to right) $\theta = 65°, 90°$ and $111°$ respectively. Time increases from the top to the bottom: $Gt = 0, 0.2136, 0.4272, 0.8544, 1.7088$

In Fig 4.3, the simulation results for receding angles and advancing angles were presented. The maximum relative deviation for receding angle is 5.9%, achieving at $111°$ and the maximum relative deviation for advancing angle is 41.6%, achieving at $65°$. Overall, we report a good agreement for the receding angle, but not for the advancing angle.

The wetting boundary condition that we applied was,

$$\phi_{i,j} = \frac{1}{a}\left(1 + a - \sqrt{(1+a)^2 - 4a\phi_{i,j+1}}\right) - \phi_{i,j+1} \tag{4.2}$$

where $a = h\Theta$ with $\Theta = -\sqrt{2\beta/\kappa}cos\theta$.

For each single time step, we put the desirable contact angle into calculation and that led to the further update of the particle distributions in the entire system. For static contact angle simulation cases as introduced in Chapter 3, the desirable contact angle was specified each time step and the final equilibrium was achieved until the boundary condition was satisfied. For the cases introduced in this chapter, however, using initial contact angle as an input to the wetting boundary condition might lead to underestimation of the actual contact angle. The simulated contact angle generally have the tendency to be closer to the initial contact angle, as shown

for case $\theta = 65°$ and $90°$, than the actual contact angles are. In other words, the development of the contact angle was supposed to be independent of the initial contact angle, and that is probably the reason why our model cannot preciously capture the contact line motion and dynamic contact angle. Similar conclusions have also been drawn by (Derksen and Komrakova, 2019).

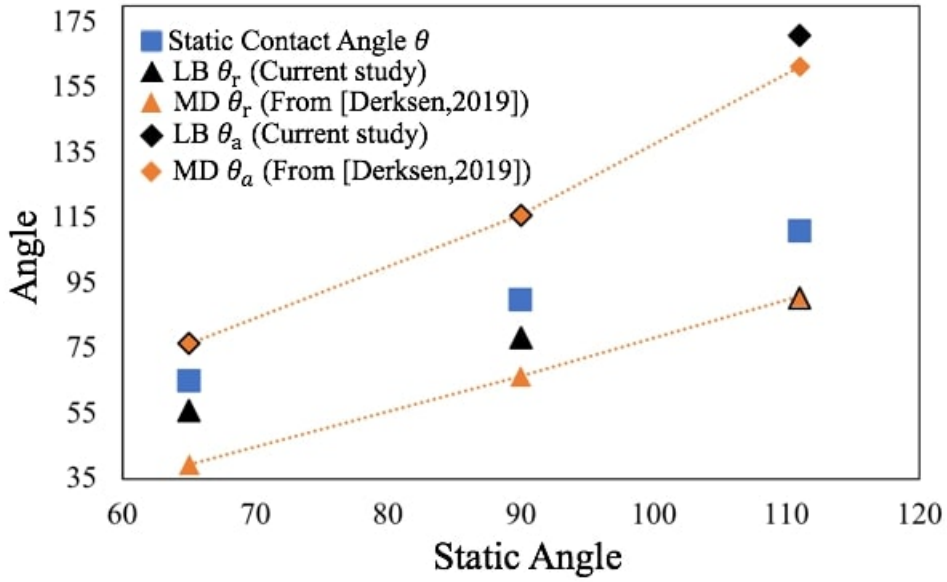

Figure 4.3: Comparison of receding angle θ_r and advancing angle θ_a in current lattice Boltzmann method study and results adapted from (Derksen and Komrakova, 2019)

4.4 Conclusions

The simulations of a droplet sliding in a simple shear flow were performed, so as to explore method's capability to capture the contact line motion. The numerical findings of the present work were compared to the reference data obtained from the molecular dynamics simulations in (Derksen and Komrakova, 2019). The comparison showed a reasonable prediction for receding angles, but not for the advancing angles. The participation of initial contact angle in the implementation of wetting boundary condition might help to explain the huge deviation, therefore further modifications are needed in order to have an independent circulation scheme for the numerical simulation of contact line motion capturing.

Chapter 5

Conclusions and Future Work

5.1 Conclusions

In this study, we developed a Fortran code from scratch to numerically study the behaviour of a liquid drop on a solid surface. A diffuse interface method was chosen and a phase-field equation was coupled with the continuity and Navier-Stokes equations to solve the flow field. A lattice Boltzmann method proposed by (Mitchell et al., 2018) was used to solve the macroscopic equations and a two-dimensional implementation of wetting boundary condition proposed by (Fakhari and Bolster, 2017) was extended to the three-dimensional cases.

The overarching focus of this project is to study the surface wetting phenomenon and contact line motion, so as to obtain a thorough understanding of a multiphase system and drop-wall interaction, as exist in many emulsion systems. Two distinct cases were preformed to study the capability of the applied model to capture the static contact angle and contact line motion, respectively; and discussions were also provided to analyse the deviation between the numerical results and reference data.

In Chapter 3, we first placed a semi-circular droplet on a solid surface and assessed the ability of the method to recover the static equilibrium contact angle achieved at different characteristics of the solid surface (from hydrophilic to hydrophobic). The deviation between the numerical and theoretical predictions of the maximum height of the drop at the equilibrium state is about 3.3%. The maximum deviation in terms of contact angle is 4.3%.

Then in Chapter 4, the simulations of a droplet sliding in a simple shear flow were performed and to explore method's capability to capture the contact line motion. The numerical findings of the present work were compared to the reference data obtained by molecular dynamics simulations (Derksen and Komrakova, 2019). The

comparison showed a reasonable prediction for receding angles, but not for the advancing angles. The possible reason behind this might be the participation of initial contact angle in the wetting boundary condition.

The current implementation of the wetting boundary condition is not ideal because it provided less accurate results when comes to the study of contact line motion. However, our applied diffuse interface phase-field LBM is powerful and the applied wetting boundary conditions give us very nice prediction for static contact angle and a satisfying prediction for dynamic contact angle. All the aforementioned advantages give us a nice starting point for future study.

5.2 Future Work

The promising of the current model motivates further study so as to perform more physically reasonable cases which allows us to directly apply into industry application. As for the future work,

- The current implementation of the wetting boundary condition needs to be further modified as it relies on the initial specified contact angle. The detailed reason has been provided in chapter 4.3. During this study, we noticed that no matter the macroscopic wetting boundary condition in eq.(2.35) or our implementation in eq.(2.38), the equations involve initial contact angle θ. Perhaps a entirely new form of wetting boundary condition for capturing the contact motion line is needed.

- The current simulation scheme should be further studied to acquire the ability to simulate a system with high density and viscosity ratio to gain more generality (gas-liquid-solid system, as an example). Many pore-scaled phenomena in industry is accomplished in gas-liquid-solid system, like the CO_2 storage (Saraji et al., 2013).

- The study of interface thickness ξ needs to be done to make sure our simulation result is well aligned with the theoretical ones. As mentioned in chapter 1.2, the choice is the interface thickness is extremely important and inappropriate value might lead to inaccuracy. Due to the time limitation, we adapted the interface thickness value from a previous study (Fakhari and Bolster, 2017), thus further study is required.

- The dimension convertion from lattice units to physical units (SI units, for instance) should be further studied, especially when the system can be applied to simulate the gas-liquid-solid system. By then, a lot of experimental data will be available, which calls for the consistency between two dimensions.

Bibliography

S Arirachakaran, KD Oglesby, MS Malinowsky, O Shoham, JP Brill, et al. An analysis of oil/water flow phenomena in horizontal pipes. In *SPE Production Operations Symposium*. Society of Petroleum Engineers, 1989.

Yan Ba, Haihu Liu, Qing Li, Qinjun Kang, and Jinju Sun. Multiple-relaxation-time color-gradient lattice boltzmann model for simulating two-phase flows with high density ratio. *Physical Review E*, 94(2):023310, 2016.

VE Badalassi, HD Ceniceros, and Sanjoy Banerjee. Computation of multiphase systems with phase field models. *Journal of Computational Physics*, 190(2):371–397, 2003.

John C Berg. *An introduction to interfaces & colloids: the bridge to nanoscience*. World Scientific, 2010.

Deepali N Bhate, Ashish Kumar, and Allan F Bower. Diffuse interface model for electromigration and stress voiding. *Journal of Applied Physics*, 87(4):1712–1721, 2000.

AJ Briant and JM Yeomans. Lattice boltzmann simulations of contact line motion. ii. binary fluids. *Physical Review E*, 69(3):031603, 2004.

F Brochard-Wyart and PG De Gennes. Dynamics of partial wetting. *Advances in colloid and interface science*, 39:1–11, 1992.

Pao-Hsiung Chiu and Yan-Ting Lin. A conservative phase field method for solving incompressible two-phase flows. *Journal of Computational Physics*, 230(1):185–204, 2011.

Joël De Coninck and Terence D Blake. Wetting and molecular dynamics simulations of simple liquids. *Annu. Rev. Mater. Res.*, 38:1–22, 2008.

Pierre-Gilles De Gennes, Françoise Brochard-Wyart, and David Quéré. *Capillarity and wetting phenomena: drops, bubbles, pearls, waves*. Springer Science & Business Media, 2013.

JJ Derksen. Droplets sliding over shearing surfaces studied by molecular dynamics. *AIChE Journal*, 61(11):4020–4027, 2015.

JJ Derksen and AE Komrakova. Multiscale simulations of sliding droplets. *Acta Mechanica*, 230(2):657–666, 2019.

JL Desmond, K Juhl, Tue Hassenkam, Susan Louise Svane Stipp, TR Walsh, and PM Rodger. Organic-silica interactions in saline: elucidating the structural influence of calcium in low-salinity enhanced oil recovery. *Scientific reports*, 7(1): 10944, 2017.

Hang Ding and Peter DM Spelt. Wetting condition in diffuse interface simulations of contact line motion. *Physical Review E*, 75(4):046708, 2007.

Hang Ding, Peter DM Spelt, and Chang Shu. Diffuse interface model for incompressible two-phase flows with large density ratios. *Journal of Computational Physics*, 226(2):2078–2095, 2007.

Jens Eggers. Contact line motion for partially wetting fluids. *Physical review E*, 72 (6):061605, 2005.

Amir Faghri and Yuwen Zhang. *Transport phenomena in multiphase systems*. Elsevier, 2006.

Abbas Fakhari and Diogo Bolster. Diffuse interface modeling of three-phase contact line dynamics on curved boundaries: A lattice boltzmann model for large density and viscosity ratios. *Journal of Computational Physics*, 334:620–638, 2017.

Abbas Fakhari and Taehun Lee. Multiple-relaxation-time lattice boltzmann method for immiscible fluids at high reynolds numbers. *Physical Review E*, 87(2):023304, 2013.

Abbas Fakhari and Mohammad H Rahimian. Phase-field modeling by the method of lattice boltzmann equations. *Physical Review E*, 81(3):036707, 2010.

Abbas Fakhari, Martin Geier, and Diogo Bolster. A simple phase-field model for interface tracking in three dimensions. *Computers & Mathematics with Applications*, 2016a.

Abbas Fakhari, Martin Geier, and Taehun Lee. A mass-conserving lattice boltzmann method with dynamic grid refinement for immiscible two-phase flows. *Journal of Computational Physics*, 315:434–457, 2016b.

Abbas Fakhari, Diogo Bolster, and Li-Shi Luo. A weighted multiple-relaxation-time lattice boltzmann method for multiphase flows and its application to partial coalescence cascades. *Journal of Computational Physics*, 341:22–43, 2017a.

Abbas Fakhari, Travis Mitchell, Christopher Leonardi, and Diogo Bolster. Improved locality of the phase-field lattice-boltzmann model for immiscible fluids at high density ratios. *Physical Review E*, 96(5):053301, 2017b.

Joel H Ferziger and Milovan Peric. *Computational methods for fluid dynamics*. Springer Science & Business Media, 2012.

Daan Frenkel and Berend Smit. Understanding molecular simulation: From algorithms to applications, 2002.

Martin Geier, Abbas Fakhari, and Taehun Lee. Conservative phase-field lattice boltzmann model for interface tracking equation. *Physical Review E*, 91(6):063309, 2015.

Mark Geoghegan and Georg Krausch. Wetting at polymer surfaces and interfaces. *Progress in Polymer Science*, 28(2):261–302, 2003.

Robert J Good. Contact angle, wetting, and adhesion: a critical review. *Journal of adhesion science and technology*, 6(12):1269–1302, 1992.

Karlheinz Graf, Michael Kappl, et al. *Physics and chemistry of interfaces*. John Wiley & Sons, 2006.

William D Gropp, William Gropp, Ewing Lusk, and Anthony Skjellum. *Using MPI: portable parallel programming with the message-passing interface*, volume 1. MIT press, 1999.

Liu Gui-rong. *Smoothed particle hydrodynamics: a meshfree particle method*. World Scientific, 2003.

Andrew K Gunstensen, Daniel H Rothman, Stéphane Zaleski, and Gianluigi Zanetti. Lattice boltzmann model of immiscible fluids. *Physical Review A*, 43(8):4320, 1991.

Axel Günther and Klavs F Jensen. Multiphase microfluidics: from flow characteristics to chemical and materials synthesis. *Lab on a Chip*, 6(12):1487–1503, 2006.

Zhaoli Guo, Chuguang Zheng, and Baochang Shi. Force imbalance in lattice boltzmann equation for two-phase flows. *Physical Review E*, 83(3):036707, 2011.

Chang Han. *Multiphase flow in polymer processing*. Elsevier, 2012.

Xiaoyi He, Shiyi Chen, and Raoyang Zhang. A lattice boltzmann scheme for incompressible multiphase flow and its application in simulation of rayleigh–taylor instability. *Journal of Computational Physics*, 152(2):642–663, 1999.

Paul C Hiemenz and Raj Rajagopalan. *Principles of Colloid and Surface Chemistry, revised and expanded*. CRC press, 1997.

PJ Hoogerbrugge and JMVA Koelman. Simulating microscopic hydrodynamic phenomena with dissipative particle dynamics. *EPL (Europhysics Letters)*, 19(3): 155, 1992.

Jun-Jie Huang, Haibo Huang, and Xinzhu Wang. Wetting boundary conditions in numerical simulation of binary fluids by using phase-field method: some comparative studies and new development. *International Journal for Numerical Methods in Fluids*, 77(3):123–158, 2015.

David Jacqmin. Calculation of two-phase navier–stokes flows using phase-field modeling. *Journal of Computational Physics*, 155(1):96–127, 1999.

David Jacqmin. Contact-line dynamics of a diffuse fluid interface. *Journal of Fluid Mechanics*, 402:57–88, 2000.

Leila Jahanshaloo, Nor Azwadi Che Sidik, Alireza Fazeli, and Mahmoud Pesaran HA. An overview of boundary implementation in lattice boltzmann method for computational heat and mass transfer. *International Communications in Heat and Mass Transfer*, 78:1–12, 2016.

D Jamet, O Lebaigue, N Coutris, and JM Delhaye. The second gradient method for the direct numerical simulation of liquid–vapor flows with phase change. *Journal of Computational Physics*, 169(2):624–651, 2001.

Vivien M Kendon, Michael E Cates, Ignacio Pagonabarraga, J-C Desplat, and Peter Bladon. Inertial effects in three-dimensional spinodal decomposition of a symmet-

ric binary fluid mixture: a lattice boltzmann study. *Journal of Fluid Mechanics*, 440:147–203, 2001.

VV Khatavkar, PD Anderson, and HEH Meijer. On scaling of diffuse–interface models. *Chemical engineering science*, 61(8):2364–2378, 2006.

Timm Krüger, Halim Kusumaatmaja, Alexandr Kuzmin, Orest Shardt, Goncalo Silva, and Erlend Magnus Viggen. The lattice boltzmann method. *Springer International Publishing*, 10:978–3, 2017.

Anand Kumar. Isotropic finite-differences. *Journal of Computational Physics*, 201 (1):109–118, 2004.

Halim Kusumaatmaja, Ewan J Hemingway, and Suzanne M Fielding. Moving contact line dynamics: from diffuse to sharp interfaces. *Journal of Fluid Mechanics*, 788:209–227, 2016.

Anthony JC Ladd. Numerical simulations of particulate suspensions via a discretized boltzmann equation. part 1. theoretical foundation. *Journal of fluid mechanics*, 271:285–309, 1994.

Pierre Lallemand and Li-Shi Luo. Theory of the lattice boltzmann method: Dispersion, dissipation, isotropy, galilean invariance, and stability. *Physical Review E*, 61(6):6546, 2000.

Pierre Lambert. *Surface tension in microsystems*. Springer, 2013.

Kock-Yee Law and Hong Zhao. *Surface wetting: characterization, contact angle, and fundamentals*. Springer Switzerland, 2016.

Sébastien Leclaire, Nicolas Pellerin, Marcelo Reggio, and Jean-Yves Trépanier. An approach to control the spurious currents in a multiphase lattice boltzmann method and to improve the implementation of initial condition. *International Journal for Numerical Methods in Fluids*, 77(12):732–746, 2015.

Sébastien Leclaire, Kamilia Abahri, Rafik Belarbi, and Rachid Bennacer. Modeling of static contact angles with curved boundaries using a multiphase lattice boltzmann method with variable density and viscosity ratios. *International Journal for Numerical Methods in Fluids*, 82(8):451–470, 2016.

Taehun Lee and Lin Liu. Lattice boltzmann simulations of micron-scale drop impact on dry surfaces. *Journal of Computational Physics*, 229(20):8045–8063, 2010.

Q Li, KH Luo, YJ Gao, and YL He. Additional interfacial force in lattice boltzmann models for incompressible multiphase flows. *Physical Review E*, 85(2):026704, 2012.

Yibao Li, Jung-Il Choi, and Junseok Kim. A phase-field fluid modeling and computation with interfacial profile correction term. *Communications in Nonlinear Science and Numerical Simulation*, 30(1-3):84–100, 2016.

Haihu Liu, Albert J Valocchi, and Qinjun Kang. Three-dimensional lattice boltzmann model for immiscible two-phase flow simulations. *Physical Review E*, 85(4): 046309, 2012.

Haihu Liu, Albert J Valocchi, Yonghao Zhang, and Qinjun Kang. Lattice boltzmann phase-field modeling of thermocapillary flows in a confined microchannel. *Journal of Computational Physics*, 256:334–356, 2014.

Minglin Ma and Randal M Hill. Superhydrophobic surfaces. *Current opinion in colloid & interface science*, 11(4):193–202, 2006.

Rui Ma, Xun Zhou, Bo Dong, Weizhong Li, and Jing Gong. Simulation of impacting process of a saturated droplet upon inclined surfaces by lattice boltzmann method. *International Journal of Heat and Fluid Flow*, 71:1–12, 2018.

Anatoly Malevanets and Raymond Kapral. Mesoscopic model for solvent dynamics. *The Journal of chemical physics*, 110(17):8605–8613, 1999.

Anatoly Malevanets and Raymond Kapral. Solute molecular dynamics in a mesoscale solvent. *The Journal of Chemical Physics*, 112(16):7260–7269, 2000.

Sean McKee, Murilo F Tomé, Valdemir G Ferreira, José A Cuminato, Antonio Castelo, FS Sousa, and Norberto Mangiavacchi. The mac method. *Computers & Fluids*, 37(8):907–930, 2008.

Shahab Mirjalili, Suhas S Jain, and Micheal Dodd. Interface-capturing methods for two-phase flows: An overview and recent developments. *Center for Turbulence Research Annual Research Briefs*, pages 117–135, 2017.

T Mitchell, C Leonardi, and A Fakhari. Development of a three-dimensional phase-field lattice boltzmann method for the study of immiscible fluids at high density ratios. *International Journal of Multiphase Flow*, 107:1–15, 2018.

F Moukalled, L Mangani, M Darwish, et al. The finite volume method in computational fluid dynamics. *An advanced introduction with OpenFoam® and Matlab®. Nueva York: Springer. Recuperado de http://www. gidropraktikum. narod. ru/Moukalled-et-al-FVM-OpenFOAM-Matlab. pdf*, 2016.

R Robert Nourgaliev, Truc-Nam Dinh, Theo G Theofanous, and D Joseph. The lattice boltzmann equation method: theoretical interpretation, numerics and implications. *International Journal of Multiphase Flow*, 29(1):117–169, 2003.

Stanley Osher and Ronald P Fedkiw. Level set methods: an overview and some recent results. *Journal of Computational physics*, 169(2):463–502, 2001.

Charles S Peskin. The immersed boundary method. *Acta numerica*, 11:479–517, 2002.

Len M Pismen and Yves Pomeau. Disjoining potential and spreading of thin liquid layers in the diffuse-interface model coupled to hydrodynamics. *Physical Review E*, 62(2):2480, 2000.

CM Pooley, H Kusumaatmaja, and JM Yeomans. Contact line dynamics in binary lattice boltzmann simulations. *Physical Review E*, 78(5):056709, 2008.

Rashmi Ramadugu, Sumesh P Thampi, Ronojoy Adhikari, Sauro Succi, and Santosh Ansumali. Lattice differential operators for computational physics. *EPL (Europhysics Letters)*, 101(5):50006, 2013.

J-P Rivet and Jean-Pierre Boon. *Lattice gas hydrodynamics*, volume 11. Cambridge University Press, 2005.

John Shipley Rowlinson and Benjamin Widom. *Molecular theory of capillarity*. Courier Corporation, 2013.

Soheil Saraji, Lamia Goual, Mohammad Piri, and Henry Plancher. Wettability of supercritical carbon dioxide/water/quartz systems: Simultaneous measurement of contact angle and interfacial tension at reservoir conditions. *Langmuir*, 29(23): 6856–6866, 2013.

Xiaowen Shan and Hudong Chen. Lattice boltzmann model for simulating flows with multiple phases and components. *Physical Review E*, 47(3):1815, 1993.

Xiaowen Shan and Gary Doolen. Multicomponent lattice-boltzmann model with interparticle interaction. *Journal of Statistical Physics*, 81(1-2):379–393, 1995.

JJ Sheng. Critical review of low-salinity waterflooding. *Journal of Petroleum Science and Engineering*, 120:216–224, 2014.

Peter DM Spelt. A level-set approach for simulations of flows with multiple moving contact lines with hysteresis. *Journal of Computational Physics*, 207(2):389–404, 2005.

Ying Sun and Christoph Beckermann. Sharp interface tracking using the phase-field equation. *Journal of Computational Physics*, 220(2):626–653, 2007.

Mark Sussman and Elbridge Gerry Puckett. A coupled level set and volume-of-fluid method for computing 3d and axisymmetric incompressible two-phase flows. *Journal of computational physics*, 162(2):301–337, 2000.

Michael R Swift, WR Osborn, and JM Yeomans. Lattice boltzmann simulation of nonideal fluids. *Physical review letters*, 75(5):830, 1995.

Sumesh P Thampi, Santosh Ansumali, Ronojoy Adhikari, and Sauro Succi. Isotropic discrete laplacian operators from lattice hydrodynamics. *Journal of Computational Physics*, 234:1–7, 2013.

Grétar Tryggvason, Bernard Bunner, Asghar Esmaeeli, Damir Juric, N Al-Rawahi, W Tauber, J Han, S Nas, and Y-J Jan. A front-tracking method for the computations of multiphase flow. *Journal of computational physics*, 169(2):708–759, 2001.

Grétar Tryggvason, Ruben Scardovelli, and Stéphane Zaleski. *Direct numerical simulations of gas–liquid multiphase flows*. Cambridge University Press, 2011.

S Van der Graaf, T Nisisako, CGPH Schroen, RGM Van Der Sman, and RM Boom. Lattice boltzmann simulations of droplet formation in a t-shaped microchannel. *Langmuir*, 22(9):4144–4152, 2006.

Zhaoyuan Wang, Jianming Yang, Bonguk Koo, and Frederick Stern. A coupled level set and volume-of-fluid method for sharp interface simulation of plunging breaking waves. *International Journal of Multiphase Flow*, 35(3):227–246, 2009.

Walter Wick. *A drop of water: A book of science and wonder*. Scholastic New York, NY, 1997.

Xianmin Xu, Yana Di, and Haijun Yu. Sharp-interface limits of a phase-field model with a generalized navier slip boundary condition for moving contact lines. *Journal of Fluid Mechanics*, 849:805–833, 2018.

Takashi Yabe, Feng Xiao, and Takayuki Utsumi. The constrained interpolation profile method for multiphase analysis. *Journal of Computational physics*, 169 (2):556–593, 2001.

P Yue and JJ Feng. Can diffuse-interface models quantitatively describe moving contact lines? *The European Physical Journal Special Topics*, 197(1):37, 2011.

XB Zhou and J Th M De Hosson. Influence of surface roughness on the wetting angle. *Journal of materials research*, 10(8):1984–1992, 1995.

YQ Zu and S He. Phase-field-based lattice boltzmann model for incompressible binary fluid systems with density and viscosity contrasts. *Physical Review E*, 87 (4):043301, 2013.

Appendix A

WMRT transformation matrix

The orthogonal transformation matrix $\mathbf{M}$ is adapted from WMRT(weighted-multiple-relaxation-time) scheme, proposed by Fakhari et al (Fakhari et al., 2017a).

$$
\mathbf{M} = \begin{pmatrix}
1 & 1 & 1 & 1 & 1 & 1 & 1 & 1 & 1 & 1 & 1 & 1 & 1 & 1 & 1 & 1 & 1 & 1 & 1 & 1 & 1 & 1 & 1 & 1 & 1 \\
0 & 1 & -1 & 0 & 0 & 0 & 0 & 1 & -1 & 1 & -1 & 1 & -1 & 1 & -1 & 1 & -1 & 1 & -1 & 1 & -1 & 1 & -1 & 0 & 0 & 0 & 0 \\
0 & 0 & 0 & 1 & -1 & 0 & 0 & 1 & 1 & -1 & -1 & 1 & 1 & -1 & -1 & 1 & 1 & -1 & -1 & 0 & 0 & 0 & 0 & 1 & -1 & 1 & -1 \\
0 & 0 & 0 & 0 & 0 & 1 & -1 & 1 & 1 & 1 & 1 & -1 & -1 & -1 & -1 & 0 & 0 & 0 & 0 & 1 & 1 & -1 & -1 & 1 & 1 & -1 & -1 \\
0 & 0 & 0 & 0 & 0 & 0 & 0 & 1 & -1 & -1 & 1 & 1 & -1 & -1 & 1 & 1 & -1 & -1 & 1 & 0 & 0 & 0 & 0 & 0 & 0 & 0 & 0 \\
0 & 0 & 0 & 0 & 0 & 0 & 0 & 1 & 1 & -1 & -1 & -1 & -1 & 1 & 1 & 0 & 0 & 0 & 0 & 0 & 0 & 0 & 0 & 1 & -1 & -1 & 1 \\
0 & 0 & 0 & 0 & 0 & 0 & 0 & 1 & -1 & 1 & -1 & -1 & 1 & -1 & 1 & 0 & 0 & 0 & 0 & 1 & -1 & -1 & 1 & 0 & 0 & 0 & 0 \\
0 & 2 & 2 & -1 & -1 & -1 & -1 & 0 & 0 & 0 & 0 & 0 & 0 & 0 & 0 & 1 & 1 & 1 & 1 & 1 & 1 & 1 & 1 & -2 & -2 & -2 & -2 \\
0 & 0 & 0 & 1 & 1 & -1 & -1 & 0 & 0 & 0 & 0 & 0 & 0 & 0 & 0 & 1 & 1 & 1 & 1 & -1 & -1 & -1 & -1 & 0 & 0 & 0 & 0 \\
-1 & 0 & 0 & 0 & 0 & 0 & 0 & 2 & 2 & 2 & 2 & 2 & 2 & 2 & 2 & 1 & 1 & 1 & 1 & 1 & 1 & 1 & 1 & 1 & 1 & 1 & 1 \\
0 & -2 & 2 & 0 & 0 & 0 & 0 & 4 & -4 & 4 & -4 & 4 & -4 & 4 & -4 & 1 & -1 & 1 & -1 & 1 & -1 & 1 & -1 & 0 & 0 & 0 & 0 \\
0 & 0 & 0 & -2 & 2 & 0 & 0 & 4 & 4 & -4 & -4 & 4 & 4 & -4 & -4 & 1 & 1 & -1 & -1 & 0 & 0 & 0 & 0 & 1 & -1 & 1 & -1 \\
0 & 0 & 0 & 0 & 0 & -2 & 2 & 4 & 4 & 4 & 4 & -4 & -4 & -4 & -4 & 0 & 0 & 0 & 0 & 1 & 1 & -1 & -1 & 1 & 1 & -1 & -1 \\
0 & 0 & 0 & 0 & 0 & 0 & 0 & 0 & 0 & 0 & 0 & 0 & 0 & 0 & 0 & 1 & -1 & 1 & -1 & -1 & 1 & -1 & 1 & 0 & 0 & 0 & 0 \\
0 & 0 & 0 & 0 & 0 & 0 & 0 & 0 & 0 & 0 & 0 & 0 & 0 & 0 & 0 & -1 & -1 & 1 & 1 & 0 & 0 & 0 & 0 & 1 & -1 & 1 & -1 \\
0 & 0 & 0 & 0 & 0 & 0 & 0 & 0 & 0 & 0 & 0 & 0 & 0 & 0 & 0 & 0 & 0 & 0 & 0 & 1 & 1 & -1 & -1 & -1 & -1 & 1 & 1 \\
0 & 0 & 0 & 0 & 0 & 0 & 0 & 1 & -1 & -1 & 1 & -1 & 1 & 1 & -1 & 0 & 0 & 0 & 0 & 0 & 0 & 0 & 0 & 0 & 0 & 0 & 0 \\
1 & -1 & -1 & -1 & -1 & -1 & -1 & 4 & 4 & 4 & 4 & 4 & 4 & 4 & 4 & 0 & 0 & 0 & 0 & 0 & 0 & 0 & 0 & 0 & 0 & 0 & 0 \\
0 & -2 & -2 & 1 & 1 & 1 & 1 & 0 & 0 & 0 & 0 & 0 & 0 & 0 & 0 & 2 & 2 & 2 & 2 & 2 & 2 & 2 & 2 & -4 & -4 & -4 & -4 \\
0 & 0 & 0 & -1 & -1 & 1 & 1 & 0 & 0 & 0 & 0 & 0 & 0 & 0 & 0 & 2 & 2 & 2 & 2 & -2 & -2 & -2 & -2 & 0 & 0 & 0 & 0 \\
0 & 0 & 0 & 0 & 0 & 0 & 0 & 2 & -2 & -2 & 2 & 2 & -2 & -2 & 2 & -1 & 1 & 1 & -1 & 0 & 0 & 0 & 0 & 0 & 0 & 0 & 0 \\
0 & 0 & 0 & 0 & 0 & 0 & 0 & 2 & 2 & -2 & -2 & -2 & -2 & 2 & 2 & 0 & 0 & 0 & 0 & 0 & 0 & 0 & 0 & -1 & 1 & 1 & -1 \\
0 & 0 & 0 & 0 & 0 & 0 & 0 & 2 & -2 & 2 & -2 & -2 & 2 & -2 & 2 & 0 & 0 & 0 & 0 & -1 & 1 & 1 & -1 & 0 & 0 & 0 & 0 \\
0 & 1 & -1 & 0 & 0 & 0 & 0 & 4 & -4 & 4 & -4 & 4 & -4 & 4 & -4 & -2 & 2 & -2 & 2 & -2 & 2 & -2 & 2 & 0 & 0 & 0 & 0 \\
0 & 0 & 0 & 1 & -1 & 0 & 0 & 4 & 4 & -4 & -4 & 4 & 4 & -4 & -4 & -2 & -2 & 2 & 2 & 0 & 0 & 0 & 0 & -2 & 2 & -2 & 2 \\
0 & 0 & 0 & 0 & 0 & 1 & -1 & 4 & 4 & 4 & 4 & -4 & -4 & -4 & -4 & 0 & 0 & 0 & 0 & -2 & -2 & 2 & 2 & -2 & -2 & 2 & 2 \\
-1 & 2 & 2 & 2 & 2 & 2 & 2 & -8 & 8 & 8 & 8 & 8 & 8 & 8 & 8 & -4 & -4 & -4 & -4 & -4 & -4 & -4 & -4 & -4 & -4 & -4 & -4
\end{pmatrix}
$$

Appendix B

Boundary Treatment

For this section, we give a precise introduction to periodic boundary condition and bounce-back boundary condition. The examples are given using D2Q9 model as shown in Fig.(2.1), in order to give a clear illustration. The applications have been extended to three dimensional for the simulations in chapter 3 and chapter 4.

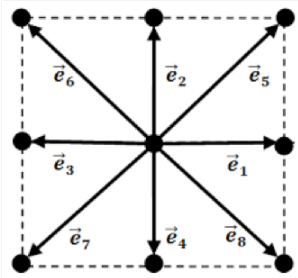

Figure 2.1: The D2Q9 model

2.1 Periodic Boundary Condition

Periodic boundary condition is designed to create a repeating flow pattern with a cyclic flow system. It is normally used in the simulations where a finite part of the flow field can be approximated by a repeating smaller flow field. Its logic is quite straightforward: the fluid leaving the domain on one side will, instantaneously, re-enter at the opposite side. Consequently, periodic boundary conditions conserve mass and momentum at all times. Periodic boundary condition is suitable and efficient for the cases like generating a fully developed flow.

The way to implement the periodic boundary condition is straightforward. As shown in 2.2, we can add additional layers of nodes at location $x_0 = x_1 - \Delta x$ and

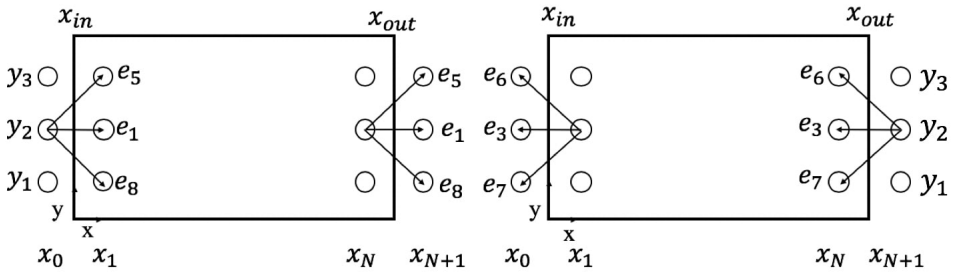

Figure 2.2: Boundary for a periodic field, nodes at location x_0 and x_{N+1} are imaginary and only added for calculation. $x_0 = x_1 - \Delta x$ and $x_{N+1} = x_N + \Delta x$

$x_{N+1} = x_N + \Delta x$ to help pass the population. The boundary of the simulated system are at $x_{in} = (x_0 + x_1)/2 = x_1 - \Delta x/2$ and $x_{out} = (x_{N+1} + x_N)/2 = x_N + \Delta x/2$. The periodic length $\mathbf{L} = x_{out} - xin = N\Delta x$. Before streaming, the population $f_\alpha^\star$ are copied into these nodes from the opposite periodic boundary of the system. During streaming, the unknown incoming populations $f_\alpha^\star$ on one side are given by those leaving the domain on the other side:

$$f_\alpha^\star(\mathbf{x}, t) = f_\alpha^\star(\mathbf{x} + \mathbf{L}, t) \tag{2.1}$$

where $\mathbf{L}$ describes the length of the flow pattern, as well as the periodicity direction. Eq.(2.1) in D2Q9 model can be implemented as

$$f_1^\star(x_0, y_2, t) = f_1^\star(x_N, y_2, t) \tag{2.2a}$$
$$f_5^\star(x_0, y_2, t) = f_5^\star(x_N, y_2, t) \tag{2.2b}$$
$$f_8^\star(x_0, y_2, t) = f_8^\star(x_N, y_2, t) \tag{2.2c}$$

For the other side, we have

$$f_3^\star(x_{N+1}, y_2, t) = f_3^\star(x_1, y_2, t) \tag{2.3a}$$
$$f_6^\star(x_{N+1}, y_2, t) = f_6^\star(x_1, y_2, t) \tag{2.3b}$$
$$f_7^\star(x_{N+1}, y_2, t) = f_7^\star(x_1, y_2, t) \tag{2.3c}$$

An alternative way to apply periodic boundary conditions is to passing the functions without the participation of the additional layers of notes. We consider the periodic boundaries of the domain as they were attached with each other as shown in 2.3. In this case, periodic boundary conditions are implemented only in streaming

process. Post-streaming distributions functions which enter the domain on the one side are replaced by the post-collision populations which leave the domain on the opposite side:

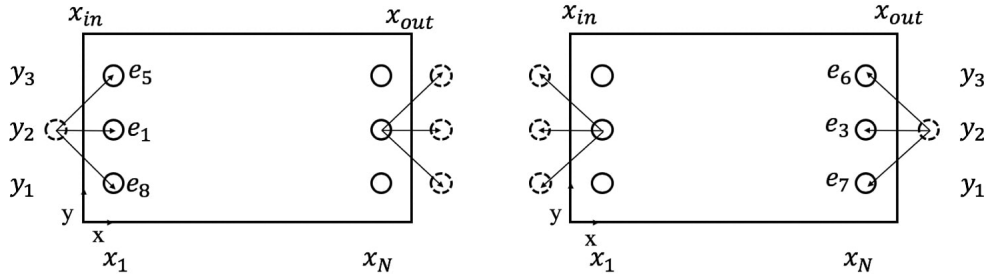

Figure 2.3: Boundary for a periodic field, nodes at location x_0 and x_{N+1} are imaginary and only added for calculation. $x_0 = x_1 - \Delta x$ and $x_{N+1} = x_N + \Delta x$

$$f_\alpha(\mathbf{x}, t + \Delta t) = f_\alpha^\star(\mathbf{x} + \mathbf{L} - e_\alpha \Delta t, t) \tag{2.4}$$

The implementation in D2Q9 model can be written as

$$f_1(x_1, y_2, t + \Delta t) = f_1^\star(x_N, y_2, t) \tag{2.5a}$$
$$f_5(x_1, y_2, t + \Delta t) = f_5^\star(x_N, y_1, t) \tag{2.5b}$$
$$f_8(x_1, y_2, t + \Delta t) = f_8^\star(x_N, y_3, t) \tag{2.5c}$$

Similarly, on the other side, we have

$$f_3(x_N, y_2, t + \Delta t) = f_3^\star(x_1, y_2, t) \tag{2.6a}$$
$$f_6(x_N, y_2, t + \Delta t) = f_6^\star(x_1, y_1, t) \tag{2.6b}$$
$$f_7(x_N, y_2, t + \Delta t) = f_7^\star(x_1, y_3, t) \tag{2.6c}$$

For our simulation, we use the alternative method as shown in eq.(2.4) wherever applicable, in order to avoid introducing new layers of nodes.

2.2 Bounce Back Boundary Condition

One of the most common boundary conditions for fluid-solid system is the no-slip boundary condition. For Lattice Boltzmann Method, the oldest but still prevalent boundary condition is bounce-back method. The principle of bounce-back method is that the fluid populations hitting a rigid wall will be bounced back to where they originally came from, as shown in Figure 2.4.

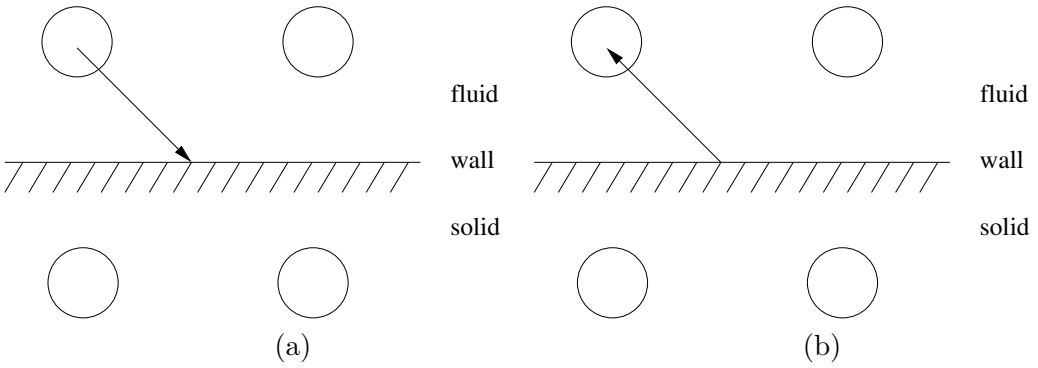

Figure 2.4: a moving particle hitting before (a) and after (b) a rigid wall

Although not straightforward at the first glance, bounce-back method follows the no-slip boundary condition in a macroscopic way. In no-slip condition, the wall is impermeable to the fluid and thus fluid transports no motion across the boundary. The total motion is thus conserved. As to bounce-back method, the fluid populations are bounced back to the original place and there is also no relative motion transportation between the fluid and the boundary.

Different from other boundary conditions, bounce-back boundary condition is stable even for a small time discretization step where $\tau \to \Delta t/2$. It is also a strict mass-conservation method that no correction terms are needed to be introduced to preserve total mass. It can obtain higher-order accuracy if surfaces are aligned with the lattice, so it is especially suitable for our case. The exact location of the no-slip boundary may be viscosity-dependent when the bounce-back scheme is used with BGK collision model, but this problem can easily be eliminated when using TRT or MRT collision model instead.

The bounce-back method can be categoried as fullway bounce-back method and halfway bounce-back method. In fullway bounce-back method, particles will travel the whole path from the boundary to the solid node and therefore the particle is bounced back during the next collision step. In halfway bounce-back method, particles travel only half of the path between the boundary and the solid node, the particle inversion thus happens at the streaming step.

The fullway bounce-back method requires solid nodes' participation where the populations are stored and then bounced back during the next collision step. Halfway bounce-back method, on the other hand, does not require solid nodes' participation since the particles only travel half path between the distance so the reflection only happens at the streaming step. Mathematically, we only need to change collision step for fullway bounce-back method or streaming step for halfway bounce-back

method.

In terms of simplicity, the fullway bounce-back method always wins over the halfway bounce-back method and the reason is quite straightforward: mathematically, we only need to check if the particle has reached the solid node or not for fullway bounce-back method, while for halfway bounce-back method, we need to tell if the particle has reached the solid node (which indicates a bounce-back condition) or it has reached a boundary or fluid node (which indicates a normal streaming step). This process may lead to huge consumption of time and memory in real implementation. However, the fullway bounce-back method can degrade the time accuracy of LB method because it requires $2\Delta t$ while the halfway bounce-back method only requires Δt to return the particle information back to the bulk. This time-delay problem would cause quite a few problems in unsteady-state problem, especially for transient problems. The halfway bounce-back method, on the other hand, does not have to consider the solid nodes, which enables it to model thin plates where the solid lattice width is infinitely small. Therefore for our simulation, we choose halfway bounce-back method over fullway bounce-back method in terms of efficiency.

Unlike the names of these two methods may imply, the locations of the boundary are both assumed as midway between solid and boundary nodes, not on the solid nodes themselves. The reason behind is that the assumption of placing boundary on the solid nodes introduces a first-order error while placing boundary in the middle is of second-order accuracy.

Similarly, in order to give a better illustration of the halfway bounce back method, we used the two dimensional D2Q9 model as an exmaple here to show all the bounce equations.

In Fig. 2.5, node x_f stands for the node inside the solid wall and node x_f stands for the node in the fluid. Populations leaving node x_f at time Δt will meet the boundary at time $t + \frac{1}{2}\Delta t$ and then bounce back at time $t + \Delta t$ to x_f. For **resting walls**, streaming steps of these populations are written as

$$f_i(x_f, t + \Delta t) = f_i^*(x_f, t) \tag{2.7}$$

In D2Q9 model, equation 2.7 can be written as (see Fig 2.5)

$$f_2(\mathbf{x}_f, t + \Delta t) = f_4^*(\mathbf{x}_f, t) \tag{2.8a}$$

$$f_5(\mathbf{x}_f, t + \Delta t) = f_7^*(\mathbf{x}_f, t) \tag{2.8b}$$

$$f_6(\mathbf{x}_f, t + \Delta t) = f_8^*(\mathbf{x}_f, t) \tag{2.8c}$$

For **moving walls**, where the bounced-back populations need to gain or lose some

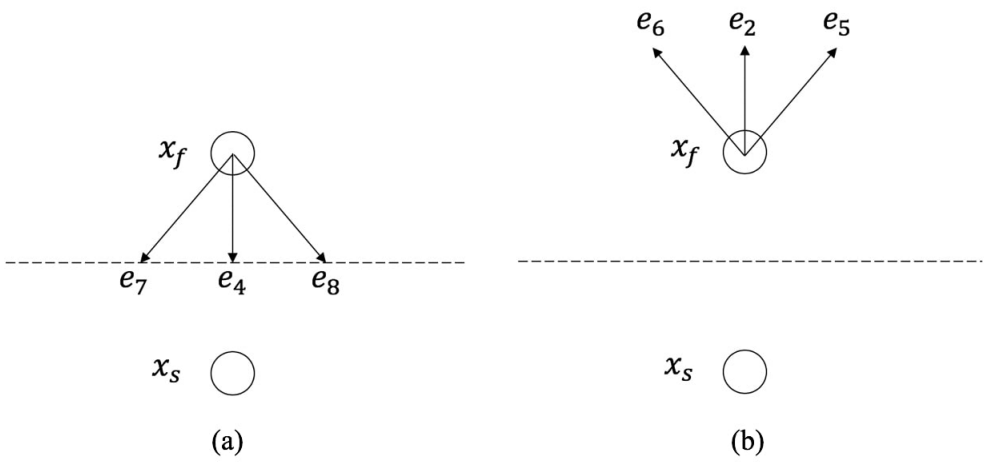

Figure 2.5: D2Q9 model before (a) and after (b) streaming at a solid wall

momentum after hitting, the right side of eq. (2.7) needs a correction, as

$$f_i(x_f, t + \Delta t) = f_i^*(x_f, t) - 2\omega_i \rho_w \frac{\mathbf{e}_i \cdot \mathbf{u}_w}{{c_s}^2} \tag{2.9}$$

where ω_i is the weights of lattice model, subscript w indicates the properties defined at the wall location $x_w = x_f + \frac{1}{2}\mathbf{c}_i \Delta t$ (the midway between the solid and fluid nodes). $\mathbf{u}_w$ is the velocity of the moving boundary. The equations are therefore revised as

$$f_2(\mathbf{x}_f, t + \Delta t) = f_4^*(\mathbf{x}_f, t) - 2\omega_4 \rho_w \frac{e_4 \cdot \mathbf{u}_w}{{c_s}^2} \tag{2.10a}$$

$$f_5(\mathbf{x}_f, t + \Delta t) = f_7^*(\mathbf{x}_f, t) - 2\omega_5 \rho_w \frac{e_5 \cdot \mathbf{u}_w}{{c_s}^2} \tag{2.10b}$$

$$f_6(\mathbf{x}_f, t + \Delta t) = f_8^*(\mathbf{x}_f, t) - 2\omega_6 \rho_w \frac{e_6 \cdot \mathbf{u}_w}{{c_s}^2} \tag{2.10c}$$

In standard LB model, the density value is usually not known at the wall. One of the solutions is to estimate ρ_w as the local fluid density ρ_b. For steady flow, the difference between ρ_w and ρ_b is normally of $O(Ma^2)$, where Ma is the local Mach number.

Appendix C

Two-dimensional Case

For this chapter, two-dimensional cases for static contact angle capturing is presented. The LB scheme is adapted from (Fakhari and Bolster, 2017), which is also a diffuse interface phase-field method, but has slight differences in terms of implementation with the one introduced by (Mitchell et al., 2018). The lattice Boltzmann formulation is provided in the following sections, as well as the two-dimensional simulation results. The macroscopic governing equations and the implementation of wetting boundary condition is identical as the three-dimensional cases, they can be found on chapter 2.1 and 2.3, respectively.

3.1 Two-dimensional lattice Boltzmann method

3.1.1 LBM for interface tracking

Particle distribution function g_α is used to recovery the interface tracking equation (Geier et al., 2015) and the equation can be written as

$$g_\alpha(\mathbf{x}+\mathbf{e}_\alpha\delta t, t+\delta t) = g_\alpha(\mathbf{x},t) - \frac{g_\alpha(\mathbf{x},t) - g_\alpha^{eq}(\mathbf{x},t)}{\tau_\phi + 1/2} \tag{3.1}$$

where τ_ϕ is the phase-field relaxation time, and $\mathbf{e}_\alpha$ is the microscopic velocity set for D2Q9 lattice, which is

$$\mathbf{e}_\alpha = c \begin{cases} (0,0), & \alpha = 0 \\ (cos(\theta_\alpha), sin(\theta_\alpha)), & \alpha = 1-4 \\ (cos(\theta_\alpha), sin(\theta_\alpha))\sqrt{2}, & \alpha = 5-8 \end{cases} \tag{3.2}$$

where $c = \delta x/\delta t = 1$ and δx and δt are the lattice length and time scale, respectively (on uniform grids$\delta x = \delta t = 1$). The weights and velocity sets for D2Q9 model can

be find in Fig. 2.1.

The equilibrium phase-field distribution function is given by

$$g^{eq} = \phi\Gamma_\alpha + \omega_\alpha \frac{M}{C_s^2}\left[\frac{4}{\xi}\phi(1-\phi)\right](\mathbf{e}_\alpha \cdot \hat{\mathbf{n}}) \tag{3.3}$$

where

$$\Gamma_\alpha = \omega_\alpha\left[1 + \frac{\mathbf{e}_\alpha \cdot \mathbf{u}}{{C_s}^2} + \frac{(\mathbf{e}_\alpha \cdot \mathbf{u})^2}{2{C_s}^4} - \frac{\mathbf{u}\cdot\mathbf{u}}{2{C_s}^2}\right] \tag{3.4}$$

$c_s = c/\sqrt{3}$ is the speed of sound in the system and ω_α is the weight coefficient set, where $\omega_0 = 4/9$, $\omega_{1-4} = 1/9$, $\omega_{5-8} = 1/36$. Mobility M is related to the phase-field relaxation time by

$$M = \tau_\phi {c_s}^2 \delta t$$

In LBM, Eq 3.1 is normally solved by a two-step collision-streaming approach as

$$g_\alpha^* = g_\alpha - \left.\frac{g_\alpha - g_\alpha^{eq}}{\tau_\phi + 1/2}\right|_{(\mathbf{x},t)} \tag{3.5a}$$

$$g_\alpha(\mathbf{x} + \mathbf{e}_\alpha\delta t, t + \delta t) = g_\alpha^* \tag{3.5b}$$

where the asterisk $(*)$ denotes the pre-streaming and post-collision state. The collision progress is using Bhatnagar-Gross-Krook (BGK) model and collision operator $\Omega_\alpha = 1/\tau_\phi$. After the streaming step, the phase field is updated by taking the zeroth moment of the phase-field distribution function

$$\phi = \sum_\alpha g_\alpha \tag{3.6}$$

the density ρ is circulated as

$$\rho = \rho_L + \phi(\rho_H - \rho_L) \tag{3.7}$$

where ρ_L and ρ_H are the densities of the light and heavy fluids, respectively. For the two-dimensional two-phase flow systems in this chapter, the phase-field variable of the heavy fluid is taken as $\phi_H = 1$, the light fluid is taken as $\phi_L = 0$, while the interface variable $\phi = 0.5$.

3.1.2 LBM for hydrodynamics

We use an improved hydrodynamic evolution equation(Fakhari and Rahimian, 2010) to update pressure and velocity fields. The lattice Boltzmann equation for incompressible multiphase flows can be written as

$$\bar{f}_\alpha(\mathbf{x}+\mathbf{e}_\alpha\delta t, t+\delta t) = \bar{f}_\alpha(\mathbf{x},t) + \Omega_\alpha(\mathbf{x},t) + F_\alpha(\mathbf{x},t) \tag{3.8}$$

where $\bar{f}_\alpha$ is the modified hydrodynamics distribution function for the incompressible fluids (He et al., 1999; Fakhari and Lee, 2013), Ω_α is the collision operator and the force term is (Fakhari et al., 2016b)

$$F_\alpha = \delta t\left[(\Gamma_\alpha-\omega_\alpha)(\rho_H-\rho_L){c_s}^2+\Gamma_\alpha\mu_\phi\right](\mathbf{e}_\alpha-\mathbf{u})\cdot\nabla\phi + \delta t\Gamma_\alpha(\mathbf{e}_\alpha-\mathbf{u})\cdot F_b \tag{3.9}$$

For hydrodynamic distribution function, we use a multiple-relaxation-time (MRT) model for the collision operator (Lallemand and Luo, 2000), which is more stable than traditional BGK model. The MRT collision operator is

$$\Omega_\alpha = \Omega_\alpha^{MRT} = -M^{-1}\hat{S}M(\bar{f}_\alpha - \bar{f}_\alpha^{eq}) \tag{3.10}$$

where the modified distribution function is defined by

$$\bar{f}_\alpha^{eq} = f_\alpha^{eq} - \frac{1}{2}F_\alpha \tag{3.11}$$

and

$$f_\alpha^{eq} = p\omega_\alpha + \rho(C_s)^2(\Gamma_\alpha-\omega_\alpha) \tag{3.12}$$

is the equilibrium distribution for nearly incompressible fluids. **M** is an orthogonal transformation, which transforms the distribution functions from physical space into moment space (Lallemand and Luo, 2000)

$$M = \begin{pmatrix} 1 & 1 & 1 & 1 & 1 & 1 & 1 & 1 & 1 \\ -4 & -1 & -1 & -1 & -1 & 2 & 2 & 2 & 2 \\ 4 & -2 & -2 & -2 & -2 & 1 & 1 & 1 & 1 \\ 0 & 1 & 0 & -1 & 0 & 1 & -1 & -1 & 1 \\ 0 & -2 & 0 & 2 & 0 & 1 & -1 & -1 & 1 \\ 0 & 0 & 1 & 0 & -1 & 1 & 1 & -1 & -1 \\ 0 & 0 & -2 & 0 & 2 & 1 & 1 & -1 & -1 \\ 0 & 1 & -1 & 1 & -1 & 0 & 0 & 0 & 0 \\ 0 & 0 & 0 & 0 & 0 & 1 & -1 & 1 & -1 \end{pmatrix} \tag{3.13}$$

$\hat{S}$ is the diagonal relaxation matrix, which is chosen to be

$$\hat{S} = diag(1, 1, 1, 1, 1, 1, 1, S_\nu, S_\nu) \tag{3.14}$$

where

$$S_\nu = \frac{1}{\tau + 1/2} \tag{3.15}$$

where τ is the hydrodynamic relaxation time (or simply the relaxation time), which is related to the kinematic viscosity of the system by $\nu = \tau {C_s}^2 \delta t$ and is calculated by using a harmonic interpolation from the phase field

$$\frac{1}{\tau} = \frac{1}{\tau_L} + \phi \left(\frac{1}{\tau_H} - \frac{1}{\tau_L} \right) \tag{3.16}$$

where τ_H and τ_L are the relaxation rates for the heavy and light fluids. After solving Eq 3.8 using a routine collision-streaming scheme, pressure and velocity fields are calculated as

$$\mathbf{u} = \frac{1}{\rho {C_s}^2} \sum_\alpha \bar{f_\alpha} \mathbf{e}_\alpha + \frac{\delta t}{2\rho} (F_s + F_b) \tag{3.17a}$$

$$p = \sum_\alpha \bar{f_\alpha} + \frac{\delta t}{2} (\rho_H - \rho L) {C_s}^2 \mathbf{u} \cdot \nabla \phi \tag{3.17b}$$

Note that velocity is updated before pressure.

Similarly, it should come to our notice that the only non-local macroscopic quantity in the proposed LB equations is the phase-field variable ϕ. Gradients and Laplacian for the phase field in Eq are calculated using second-order, isotropic centered differences (Kumar, 2004). The centered difference method is used to preserve the mass and momentum conservation. And the combination of conservative phase-field method and isotropic centered differences can attain an enough stable scheme for large ratio density and viscosity analysis as we are about to do for gas-liquid-solid system.

3.2 Validation case

2D validation case is done by putting a semi-circular droplet on solid wall. Different contact angle will then be imposed to the model and the system will develop to a new equilibrium state. The simulation is done with two phases of equal density and equal viscosity, and the simulation parameters are considered as: surface tension $\sigma = 0.01$, interface thickness $\sigma = 4.0$, Mobility $M = 0.02$ and relaxation time $\tau_g = 0.06$. The simulation domain is resolved as $100 \times 100(lu)$, the initial droplet diameter is $30(lu)$, and the initial droplet is located at (50,0). Periodic boundary condition is applied on both the left and right wall, bounce-back boundary condition is applied for top wall to achieve no-slip boundary condition and wetting boundary condition is applied on the bottom wall.

Numerical simulation results of four different non-neutral contact angles is presented in figure 3.2 and neutral condition is presented in figure 3.1.

To testify the accuracy of simulation results, recall equation 3.8, the conservation of mass leads to a height change with different contact angles imposed. The compare of analytical and numerical results are shown in fig 3.3. The maximum relative deviation is 4.26% and it is achieved at the contact angle of 150°. This level of accuracy is acceptable for these complex systems.

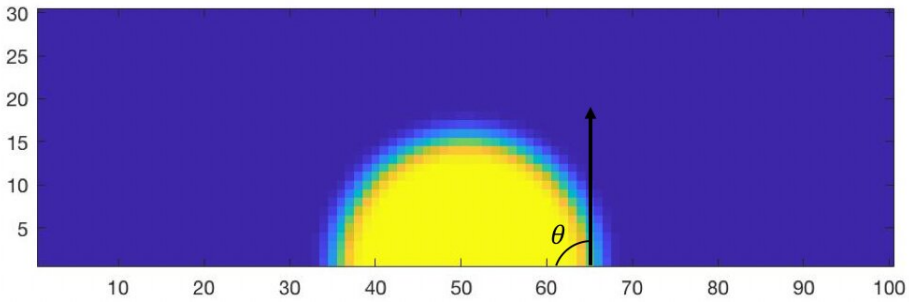

Figure 3.1: Semi-droplet equilibrium with neutral boundary condition (θ=90°)

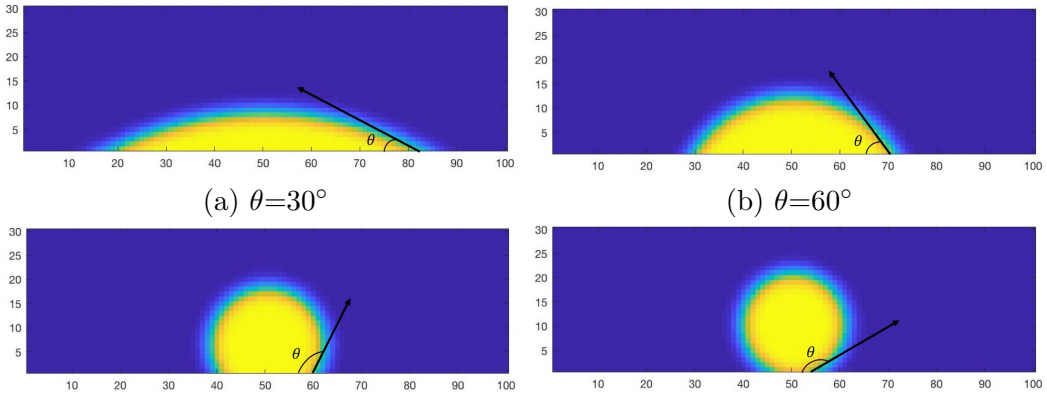

(a) θ=30° (b) θ=60°

(c) θ=120° (d) θ=150°

Figure 3.2: Equilibrium state of the drop with different contact angles

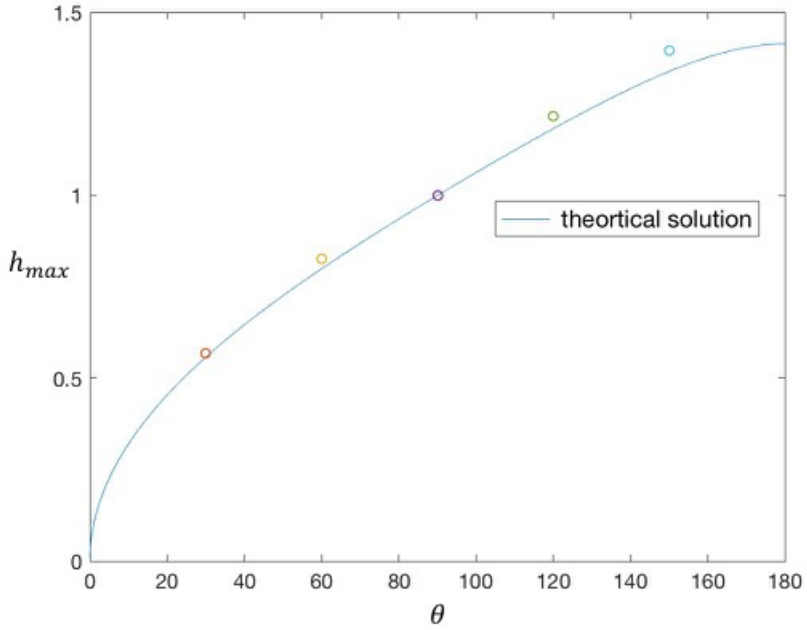

Figure 3.3: compare between analytical and numerical results

3.3 Conclusion

In this chapter, the two-dimensional cases of a droplet behaviour on a solid surface was modelled using a diffuse interface phase-field lattice Boltzmann method. The ability of the current implementation of two-dimensional wetting boundary conditions to capture the static contact angles was tested. Numerical simulation results showed a reasonable deviation with the theoretical results, which offered us a nice starting point for the further three-dimensional study.